УДК 544.42/43

Многотемпературная модель SPS реактора синтеза и уплотнения нитрида циркония

А. А. Марков

Институт проблем механики им. А.Ю. Ишлинского Российской академии наук
Россия, Москва, 119526, проспект Вернадского, д. 101-1

markov.ipm@yandex.ru

Аннотация

Модель включает температуру твердой фазы смеси Zr и ZrN, температуру газовой фазы N_2 и температуру корпуса реактора из пористого графита, температуру низкоомного слоя вольфрамового сплава к электродам которого приложена разность потенциалов. Предложена модель реактора искрового спекания SPS, который содержит канал для подачи газа. Исследованы режимы работы реактора с многостадийным потоком азота на входе в реактор, включающие предел упругости с переходом к термопластичности для пористой смеси твердых частиц с газовой фазой. Результаты удовлетворительно согласуются с экспериментальными данными.

Ключевые слова: переменная пористость, синтез нитрида циркония, SPS реактор с подачей газа, многотемпературная модель.
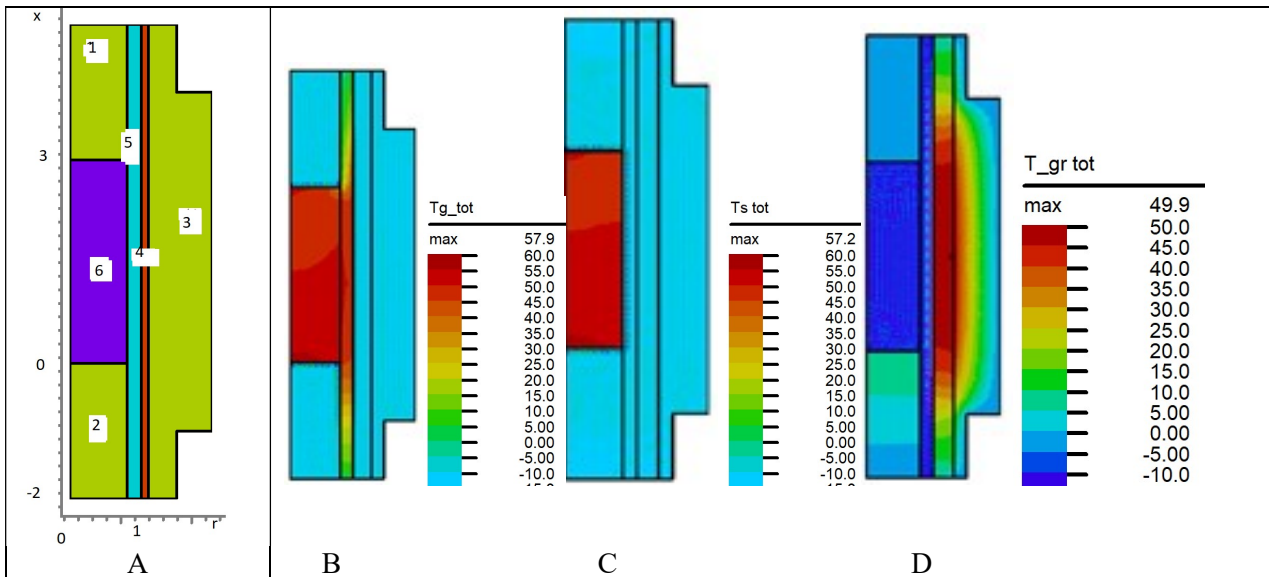

Рис. 1. Схема SPS реактора (рис. 1, A). Показана область моделирования, состоящая из зон 1−6.
Зона 1: $3 < x < 5, 0 < r < R_1$; зона 2: $-2 < x < 0,\ 0 < r < R_1$; зона 3: $-1 < x < 4,\ 1 + \delta < r < R_2$ − графитовый корпус реактора; зона 4: $-2 < x < 5,\ 1 < r < 1 + \delta$ − вольфрамовый слой; зона 5: $0 < x < 3,\ R_1 < r < 1$ − канал подачи N_2; зона 6: $0 < x < 3,\ 0 < r < R_1$ − пористая область смеси реагентов и продуктов синтеза. На рис. 1, B и рис. 1, C иллюстрируется распределение температуры газа и твердой фазы в зоне 6 в момент времени $t = 0.88$. На рис. 1, D представлено распределение температуры графитового корпуса в зонах 1,2, 3 в момент времени $t = 0.88$

Multitemperature Model of a SPS Reactor for the Synthesis and Densification of Zirconium Nitride

A. A. Markov

Ishlinskyi Institute for Problems in Mechanics, Russian Academy of Sciences (IPMech RAS), Moscow, 119526, Russia

markov.ipm@yandex.ru

Abstract

The model includes the temperature of the solid phase of the mixture of Zr, ZrN, the temperature of the gas phase N_2, the temperature of the reactor vessel made of porous graphite and the temperature of the low-resistance layer of tungsten alloy to the electrodes of which a potential difference is applied. A model of an SPS spark sintering reactor with a gas supply channel is proposed. The operating modes of a reactor with a multistage nitrogen flux at the reactor inlet, including the elastic limit with a transition from thermoelasticity model to thermoplasticity one for a porous mixture of solid particles with a gas phase, are investigated. The results are in satisfactory agreement with experimental data.

Key words: variable porosity, synthesis of zirconium nitride, SPS reactor with gas supply, multitemperature model.
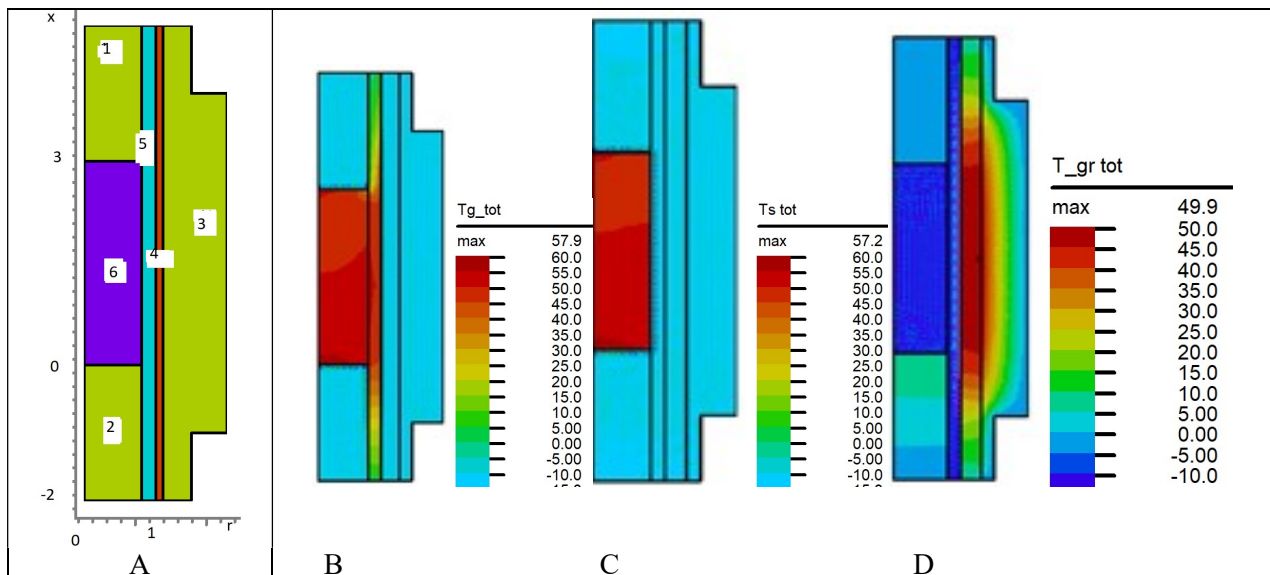
Fig. 1. Schematic of the SPS reactor (fig. 1, A). The modeling area is shown, consisting of zones 1−6. Zone 1: $3 < x < 5, 0 < r < R_1$. Zone 2: $-2 < x < 0,\ 0 < r < R_1$. Zone 3: $-1 < x < 4, 1 + \delta < r < R_2$ − graphite reactor vessel. Zone 4: $-2 < x < 5, 1 < r < 1 + \delta$ − tungsten layer. Zone 5: $0 < x < 3, R_1 < r < 1$ − feed channel of N_2. Zone 6: $0 < x < 3, 0 < r < R_1$ - porous area of a mixture of reagents and synthesis products. fig. 1, B and fig. 1, C illustrates the temperature distribution of the gas and the solid phase in zone 6 at time instance $t = 0.88$. Fig. 1, D shows the temperature distribution of a graphite body in zones 1, 2, 3 at time instance $t = 0.88$

1.   Introduction

Zirconium nitride ZrN has attracted more and more attention in the last decade due to its combination of excellent thermal, mechanical and electrical properties, high melting point, hardness and high strength characteristics. Ceramics based on zirconium nitride are used in electrical engineering, atomic materials science and manufacturing. Ceramics ZrC and ZrN are of interest for the use the materials at extremely high temperatures. Zirconium carbide ZrC and nitride ZrN exhibit desirable characteristics such as high thermal conductivity and electrical conductivity. The data presented in the literature often suffer from scatter due to differences in processing methods and the complexity of determining stoichiometry, which significantly affects the thermophysical properties [1]. However, the methods of processing these materials can change the content of impurities such as oxygen in ZrC and oxygen and carbon in ZrN. Also, zirconium nitride is used as protective wear-resistant coatings of parts in contact with aggressive media, is a substitute for uranium nitride to optimize the parameters of the nitride fuel fabrication process, which is considered for use in space power reactors [2] and advanced emergency-resistant fuels for reactors [3, 4]. Zirconium has a remarkable ability to burn in atmospheric oxygen (autoignition temperature is 250° C) with little or no smoke and at a high rate.This develops the highest temperature for metallic fuels (4650° C). Experiments were carried out on using the combustion of zirconium as a light source for pumping a laser. Zirconium and hafnium nitride are refractory ($>2500°$ C) and are close in hardness to superhard materials (24 GPa) [5, 6]. These materials, having high thermal and electrical conductivity [1], are applied in microelectronics.

To obtain ZrC and ZrN, the method of self-propagating high-temperature synthesis (SHS) [7−9] and the method of chemical vapor deposition [6, 10] were used. The method for producing zirconium nitride based on SHS by burning a mixture consisting of zirconium oxide and an energy component in the presence of a nitriding agent is carried out. In the process, the intermediate products are quenched by interrupting the combustion process in $20 \div 90$ seconds after initiation, and an activating additive of oxides nanopowder is additionally incorporated into the exothermic mixture.The synthesis of carbide and nitride materials usually involves a direct reaction with a metal, metal hydride, or metal oxide, with the metal oxide being the main precursor in spent fuel reprocessing [1].

The traditional approach to obtaining materials based on fine ZrN powders [6] separates the stages of synthesis and sintering. The resulting cakes are mechanically ground in ball mills and re-nitrided. The process is repeated until the nitride yield reaches $95 \div 98\%$.One of known method of obtaining zirconium nitride is a direct nitriding of zirconium powder. Zirconium powder is subjected to heat treatment at a temperature of $1200 \div 1600°$ C in a nitrogen environment. The disadvantages of this method are high synthesis temperatures, complex instrumentation. An expensive pure nitrogen gas have to be used. There is a known method in which hydrogenated zirconium powder forms nitride at high temperatures, about $1300 \div 1400°$ C, during 5 hours in a nitrogen atmosphere. Zirconium nitride was obtained by nitriding zirconium hydride at 1050° C for 21 h [11]. A method for producing zirconium nitride by reducing zirconium oxide with carbon black in a nitrogen atmosphere at 1300° C is also applied. The disadvantage of this method is the presence of unreacted carbon in the products, as well as the formation of a solid solution ZrN-ZrC [12]. To obtain zirconium nitride, especially pure nitrogen is used without oxygen and water impurities [1]. Another area of industrial production is the synthesis of nitrides based on a stream of pure nitrogen which passes over the mixture [13, 14]. Additionally, it was found that the densificationmechanisms of the processed powders can be changed by electric current.Thedensification mechanisms depend on the particle size, temperature and pressure [1, 7, 8, 15].

Spark plasma sintering (SPS), which is also called sintering by pulsed electric current or electric field, involvesthe passing a pulsed DC current through a graphite matrix and using rapid Joule heating, along with uniaxial pressing. The SPS is used to obtain dense samplesof nitrides. It has been established that a decrease in the yield stress of a particle material under the action of an electric current is the main mechanism for the rapid densification of conductive powders compacted

with an electric current [2, 15, 16]. The SPS has been reported to be successful in achieving cleaner grain boundaries, improved mechanical and thermoelectric properties, improved resistance to oxidation and corrosion [1]. The SPS method has the advantage of speeding up the sintering of materials in minutes compared to the hours required to other traditional densification methods such as hot pressing or pressureless sintering [11−16].

The method for the synthesis of oxides by combustion of carbon (CCSO) [17] stimulated theoretical studies [18−23]. Models of averaging based on interpenetrating continua were proposed, in which the lost detailed information on micro-scales, such as the configuration of interphase boundaries, etc., is presented in the form of heat and mass transfer coefficients. A number of papers have shown the importance of dispersion terms in the averaged equations along with molecular diffusion of heat and matter. The concentration and the heat dispersion is caused by fluctuations in mass and heat flux, while the diffusion is caused by molecular motion. Various models of thermal dispersion have been studied in [24−30].

Modeling the synthesis of materials was developed in [18−23], in the approximation of constant pore sizes, given a priori. It should be noted that the pore sizes, as a rule, are unevenly distributed in the reactor of synthesis, the pore sizes are changed in time, affecting the fluxes of heat and the mass fluxes of reagent substances and products through the porous medium. Gradients of temperature and concentration lead to a change in volume and the appearance of displacements and stresses in the solid phase. In [31−34] models of sintering and synthesis of powder mixtures of a solid phase are considered, taking into account the mutual influence of the processes of volumetric changes in the sintering process. Thermal expansion is an important feature of a composite fuel material such as UN dispersed in ZrN.

In papers [35, 36] the effect of the concentration expansion of the solid phase under conditions of interfacial heat and mass exchange is investigated. The volumetric change in the synthesis of barium titanate $BaTiO_3$ on the basis of a two-phase model of thermal and mass dispersion has been taken into account. A theoretical model is proposed that makes it possible to predict the characteristics of the combustion wave moving in the sample of variable porosity, when the surface type of combustion occurs. Simulation of the synthesis of barium titanate by the CCSO method in an axisymmetric SPS reactor [37], with a channel for gas supply and with an electrically conductive layer of a tungsten alloy for heating the mixture of reagents and initiating combustion, densification and sintering of the synthesis product was carried out. The themodel of thermoelasticity, thermoplasticity, and transition from elasticity to plasticity was considered. The formula of unsteady change of porosity in the synthesis zone at a given distribution of porosity at the initial moment of time is used [34]. The influence of variable porosity on the processes of synthesis of micron particles with thermal and mass dispersion accompanying convective and conductive heat - mass transfer has been studied. Concentration expansion of the gas phase due to gas pressure on the pore surface slows down the decrease in pores during combustion due to thermal and concentration expansion of the solid phase. Chemical transformations occur with a change in volume and are accompanied by the appearance of mechanical stresses and strains in addition to stresses and strains due to high temperature gradients.

In connection with the requirements of the industrial production of ceramics, there is a need to balance energy consumption, synthesis time and the quality of the final product. In this paper, we propose a model of an SPS reactor with a graphite shell of low porosity and with a gas supply through a channel specially located in the reactor close to the boundary of the synthesis zone filled with a finely dispersed reagent. A two-stage reactor for producing zirconium nitride based on the combustion of a mixture consisting of zirconium and a nitriding agent is considered. The stream of pure nitrogen is passed over the mixture of synthesis of nitrides. The initiation of the synthesis, densification and sintering of zirconium nitride is carried out by the time-controlled Joule heat release due to an electric current passed through the tungsten channel. The degree of nitriding is controlled by the intensity of the nitrogen flow supplied at the inlet to the reactor. To simulate the synthesis of zirconium nitride, along with densification and sintering, the results of thermal and

concentration expansion [33, 34] and the results of thermoplasticity [38−40] are used.In the present paper modeling zirconium nitride in the reactor is considered on the basis of the macroconservation equations written in dimensionless variables including the terms of thermal and mass dispersion are presented. Simulation of the synthesis of zirconium nitride by the combustion and densification method based on the model by Olevsky [39] in an axisymmetric reactor has been carried out.The results obtained show a significant effect of volumetric changes in the solid phase.The proposed model allows us to analyze the effect of] thermal and concentration expansion on the distribution of porosity in the reactor, the synthesis rate and product distribution in the synthesis zone. This paper presents the results of modeling for particle sizes exceeding microns. Note that for micron sizes of synthesized particles, the characteristic value of the Knudsen number is small and the effects of slip and temperature jumps [41] are negligible. However, for submicron sizes of particles and pores, the influence of Knudsen layers in the gas near the pore surface becomes significant and it is necessary to take into account slip effects [18−21].

2.   Theoretical analysis

2.1.   Description of the model

ZrN is characterized by a wide range of stoichiometry [5, 13, 42−47]. Nitriding was accompanied by a flow of N_2. The application of high pressure leads to an increase in the ratio of nitrogen in the powders. It is assumed that cold pressing with an increased load prior to the SPS process leads to an increase in the contact area with the particles, which leads to a decrease in the number of open pores that affect the rapid diffusion of dissociated nitrogen pathways [1, 3, 4].

Let us consider the simplest scheme for the synthesis of zirconium nitride [5, 13]

$$N_2 + 2Zr \xrightarrow[Q_1]{k_1} 2ZrN \tag{1}$$

The components of gas and solid phase are N_2 and Zr, ZrN. In reaction (1), the components of the solid phase do not mix at the molecular level, diffuse and move within the solid phase, k_1, Q_1 are reaction rate and the heat effect of combustion of zirconium [5].

Expansion factors. The governing system of equations includes the equations of conservation of mass, energy and momentum for the gas phase and the equations of thermoelasticity and thermoplasticitybased on the Duhamel−Neumann relations and themodel [38] for the solid phase.

We use for the stress tensor components the generalized Duhamel−Neumann relations of the linear theory of thermoelasticity

$$\sigma_{ij} = 2\mu_{S1}\varepsilon_{ij} + \delta_{ij}\left(\mu_{S2}\sum_k \varepsilon_{kk} - K\omega\right) \text{[48]},$$

and the relation between the invariants

$$\sum_k \sigma_{kk} = (2\mu_{S1} + 3\mu_{S2})\sum_k \varepsilon_{kk} - 3K\omega$$

following from the Duhamel−Neumann relations, where σ_{ij} are the stress tensor components and ε_{ij} are the strain tensor components depending on the expansion coefficients; μ_{S1}, μ_{S2} are the Lane coefficients; K is the isothermal module of all-round compression. We assume that the gas pressure on the pore surface is balanced by the normal stress of the solid boundary, i.e. $\sum_k \sigma_{kk} = 3p$, then

$$\sum_k \varepsilon_{kk} = (K\omega + p)\mu_S^{-1},$$

where $\mu_S = \dfrac{2}{3}\mu_{S1} + \mu_{S2}$.

If there is no external forces then $\sigma_{ii} = 0$ and, therefore $\sum\limits_k \varepsilon_{kk} = K\omega\mu_S^{-1}$. Quantity $\omega = \omega_T + \omega_g + \omega_S$ is the total coefficient of volumetric expansion, in which $\omega_T = 3\alpha_T\left[\left(-T_g/T_g^0\right)+1\right]$ is the coefficient of thermal expansion; ω_g, ω_S are the coefficients of concentration expansion of the components of the gas and solid phases. The values ω_g, ω_S are estimated using the molar volumes occupied by the components $v_{1g} = \dfrac{M_{1g}}{\rho_{1g}}$, $v_{jS} = \dfrac{M_{jS}}{\rho_{jS}}$ [31, 34].

Using the molar concentrations of the components

$$\bar{\alpha}_{iS} = \frac{1}{3}\frac{v_{iS}}{v_{1g}+v_{1S}+v_{2S}}, \quad i=1,2,$$

we arrive at the relations $\omega_g = 0$, $\omega_g = 3\alpha_{1g}\left(-B_{1g}+B_{1g}^0\right)$ and $\omega_S = 3\left[\sum\limits_{j=1}^{2}\alpha_{jS}\left(-B_{jS}+B_{jS}^0\right)\right]$, in which $B_{1g} = 1$, $B_{1g} = \dfrac{Y_{1g}}{Y_{g,tot}}$, $B_{jS} = \dfrac{Y_{jS}}{Y_{S,tot}}$, $B_{jS} = \dfrac{Y_{jS}}{Y_{1S}+Y_{2S}}$ and $Y_{jS} = \dfrac{\rho_{jS}}{M_{jS}}$, the index zero refers to the values at the initial time instance.

The variable porosity of the mixture of reagents and the product for the zirconium nitrade synthesis i taking into account the effects of thermal and concentration expansion of the components of the gas and solid phases is founnd as [34]

$$\chi(t,x,r) = \frac{\chi(0,x,r)}{\chi(0,x,r)+[1-\chi(0,x,r)][1+E(t,x,r)]}, \tag{2}$$

where $E(t,x,r) = \sum\limits_{k=1}^{3}\varepsilon_{kk}(t,x,r)$.

The notation $\chi(0,x,r) = \chi_0$ further is used. The matching condition $E(0,x,r) = 0$, $\omega_g(0,x,r) = E(0,x,r)$ follows from the initial condition. To simulate the effect of gas pressure on the pore surface, we introduce a scale ζ_p. Using the matching condition, we get

$$\zeta_p = -\frac{K}{P(0,x,r)}\left[\omega_T(0,x,r)+\omega_S(0,x,r)\right] \tag{3}$$

The governing equation of thermoplasticity for SPS. Beyond the elastic limit, the thermoplasticity model is used [48−50]. We assume that plastic deformation of the material $\dot{\gamma}$ is activated thermally, and the rate of deformation can be expressed as follows [38−40]

$$\dot{\gamma} = \dot{\gamma}_0\exp\left(\frac{-E_{pl}}{RT}\right),$$

where E_{pl} is the activation energy (kJ/mol); T is absolute temperature (K).

Further, the Olevsky model [38], based on the power-law plasticity, $\sigma(W) = A_m\cdot W^m$ for a porous viscous material is applied. The value

$$A_m = \frac{A_0 T}{r_p} \left(\frac{d}{b}\right)^p \exp\left(\frac{-E_{pl}}{RT}\right),$$

where $d = 1, b = 0.05, p = 1.1$; A_0, A_m are the creep coefficients for the power law; r_p is the particle size, $r_p \sim 5 \times 10^{-7}$; T is the absolute temperature; R is the gas constant; E_{pl} is the creep activation energy according to the power law, see [38] in detail. Further we consuder $\frac{\sigma(W)}{W} = r_p A_m^m W^{m-1}$, where W is the equivalent strain rate . The densification rate $\dot{\gamma}$ and shape change $\dot{e}$ are functions of the strain rate tensor components

$$\dot{\gamma} = \sqrt{2\left(\dot{\varepsilon}_{xy}^2 + \dot{\varepsilon}_{xz}^2 + \dot{\varepsilon}_{yz}^2\right) + \frac{2}{3}\left(\dot{\varepsilon}_x^2 + \dot{\varepsilon}_y^2 + \dot{\varepsilon}_z^2\right) - \frac{2}{3}\left(\dot{\varepsilon}_x\dot{\varepsilon}_y + \dot{\varepsilon}_x\dot{\varepsilon}_z + \dot{\varepsilon}_z\dot{\varepsilon}_y\right)} \quad [38].$$

The value of the equivalent strain rate for a porous material is determined as follows

$$W = \frac{1}{\sqrt{1-\chi}}\sqrt{\varphi\dot{\gamma}^2 + \psi\dot{e}^2},$$

where $\dot{e} = \sum_k \dot{\varepsilon}_{kk}$ is the trace of the strain rate tensor.

For a power-law strain rate equivalent to creep of a porous solid, two functions of porosity are introduced: $\varphi = (1-\chi)^2$ the normalized shear modulus and $\psi = \frac{2}{3}\frac{(1-\chi)^3}{\chi}$ the normalized bulk modulus. Based on the continuous sintering theory [38−40], the constitutive equation describing hot pressing of a nonlinear-viscous porous material with a rigid matrix is expressed as

$$\sigma_{ij} = \frac{\sigma(W)}{W}\left[\varphi\,\dot{\varepsilon}_{ij} + \left(\psi - \frac{1}{3}\varphi\right)\dot{e}\delta_{ij}\right] + P_L\delta_{ij},$$

where σ_{ij} is the stress tensor; δ_{ij} is the unit tensor; P_L is the effective stress of free sintering, which is defined as

$$P_L = \frac{3\alpha}{r_p}(1-\chi)^2,$$

where α is the surface energy; r_p is the average grain diameter. In a porous medium of a gas and a solid phase, it is necessary to take into account the gas pressure at the pore boundary P_g and external pressure P_{ex}, when simulating hot pressing, along with SPS

$$\sigma_{ij} = \frac{\sigma(W)}{W}\left[\varphi\,\dot{\varepsilon}_{ij} + \left(\psi - \frac{1}{3}\varphi\right)(P_{ex} - P_g)\delta_{ij}\right] + P_L\delta_{ij} \qquad (4)$$

We consider $\dot{\varepsilon}_r = 0$ [38] in this case for the rate of porosity decrease in densification, (also called the governing equation for nonlinear viscous densification) the following relation is valid

$$\dot{\chi} = -\left[\frac{r_p}{A_0 T}\left(\frac{b}{d}\right)^p \exp\left(\frac{-E_{pl}}{RT}\right)\right]\left(\frac{3\chi}{2}\right)^{\frac{m+1}{2m}}(1-\chi)^{\frac{m-3}{2m}}\left(\frac{\sigma_{tot}}{r_p}\right)^{\frac{1}{m}},$$

where $\sigma_{tot} = P_{tot} + P_L + \omega_T + \omega_g + \omega_S$.

The constitutive equation describing the densification of a nonlinearly viscous porous mixture of solid particles can be written in the form [38−40]

$$\dot{\chi} = -A_m^{-1}\left(\frac{3\chi}{2}\right)^{\frac{m+1}{2m}}(1-\chi)^{\frac{m-3}{2m}}\left(\frac{\sigma_{tot}}{r_p}\right)^{\frac{1}{m}}\tag{5}$$

The calculation of the change in porosity in a two-stage synthesis-densification reactor during concentration expansion based on the Duhamel − Neumn thermoelasticity relations and on the basis of the constitutive densification equation (5) was carried out using the conditional plasticity limit [48], the conditional yield strength usually means such a stress at which the permanent deformation is 0.2 %. For deformation of the radius of the particle $\left(r_P - r_P^0\right)/r_P^0 = 0.2\%$, we obtain

$$\left(\frac{V_{\lim}}{V_0}\right) = 8\times10^{-9}l_0^{-3} = 10^{-3}$$

Let us estimate the limiting value of porosity, taken as the plasticity limit at the particle radius $r_P \approx 5\times10^{-7}\,(\mathrm{m})$, volume $V_P = 4/3\,\pi r_P^3$. The number of particles in one mole of the mixture $n_P = N_A \cdot V_P/V_0\,(\mathrm{mol}^{-1})$, where Avogadro's number $N_A = 6\times10^{23}\,(\mathrm{mol}^{-1})$, $V_0 = 8\times10^{-6}$ we obtain

$$n_P = 6\times10^{23}\times125\times\frac{4}{3}\pi\times10^{-21}\times10^6\,(\mathrm{m}^3\cdot\mathrm{mol}^{-1}\cdot\mathrm{m}^{-3}),$$

$$n_P \approx 1.2\times10^{10},\quad \frac{V_g^{\lim}}{V_g^0} = \frac{V_g^0 - V_g}{V_g^0} = 10^{-3}$$

Let us denote $V_{mol} = \dfrac{(n_P\cdot V_p)}{(n_P^0\cdot V_p^0)}$, $G_0 = \dfrac{\rho_{2s}^0}{M_{2s}} - \dfrac{\rho_{1s}^0}{M_{1s}} - \dfrac{\rho_{1g}^0}{M_{1g}}$ and $G_1 = \dfrac{\rho_{2s}}{M_{2s}} - \dfrac{\rho_{1s}}{M_{1s}} - \dfrac{\rho_{1g}}{M_{1g}}$ the number of moles per unit volume of the mixture $\dfrac{(V_g^0 + V_s^0)}{(V_g + V_s)} = V_{mol}\dfrac{G_1}{G_0}$, the index zero refers to the initial moment of time. Let $\zeta = \dfrac{(1-10^{-3})(V_g^0 + V_s^0)}{(V_g + V_s)}$, then in case $V_{mol} = 1$ we get $\zeta = \dfrac{(1-10^{-3})G_1}{G_0}$.

The limiting value of porosity, according to the plasticity limit, is equal to $\chi = \zeta\chi_0$. In the computations in the range $\chi \geq \zeta\chi_0$, the thermoelasticity model is used, and for $\chi < \zeta\chi_0$ the thermoplasticity model. We introduce an indicator of the thermoplasticity mode $i_{elast}(t,x,r) = \begin{cases}1, & \chi < \zeta\chi_0 \\ 0, & \chi \geq \zeta\chi\end{cases}$, then for calculating the porosity we get

$$\chi(t,x,r) = \chi_1(t,x,r)[1 - i_{elast}(t,x,r)] + \chi_2(t,x,r)i_{elast}(t,x,r),\tag{6}$$

$$\chi_1(t,x,r) = \frac{\chi_0[1+\omega_g(t,x,r)]}{\chi_0[1+\omega_g(t,x,r)] + (1-\chi_0)[1+E(t,x,r)]},\tag{7}$$

$$\dot{\chi}_2(t,x,r) = -\left[\frac{r_p}{A_0 T}\left(\frac{b}{d}\right)^p\exp\left(\frac{-E_{pl}}{RT}\right)\right]\left(\frac{3\chi_2}{2}\right)^{\frac{m+1}{2m}}(1-\chi_2)^{\frac{m-3}{2m}}\left(\frac{\sigma_{tot}}{r_p}\right)^{\frac{1}{m}}\tag{8}$$

The dimensionless variables. We apply below the dimensionless variables, marked with a tilde as follows

$$\tilde{x}_i = \frac{x_i}{l_0}, \ \ \tilde{t} = \frac{t}{t_0}, \ \ \tilde{u}_i = \frac{u_i}{u_0}, \ \ \tilde{V}_{i,solid} = \frac{V_{i,solid}}{u_0}, \ \ \tilde{p} = \frac{p}{p_0}, \ \ u_0 = \frac{l_0}{t_0}, \ \ i = 1,2,3;$$

$$\tilde{\rho}_g = \frac{\rho_g}{\rho_0}, \ \ \tilde{\rho}_{jg} = \frac{\rho_{jg}}{\rho_0}, \ \ j = 1,2,3; \ \ \tilde{c}_{pg} = \frac{C_{pg}}{c_p}, \ \ \tilde{D} = \frac{D}{D_0}; \ \ \mu_0 = \rho_0 \nu_{air};$$

$$\rho_{1S} = \rho_{Zr}, \ \ \rho_{2S} = \rho_{ZrN}, \ \ \tilde{\rho}_{lS} = \frac{\rho_{lS}}{\rho_{0Zr}}, \ \ l = 1,2; \ \ \rho_S = \rho_{1S} + \rho_{2S},$$

$$\tilde{c}_{pg} = \frac{C_{pg}}{c_p}, \ \ \tilde{D}_m = \frac{D_m}{D_0}, \ \ \tilde{\lambda}_g = \frac{\lambda_{air}}{\lambda_0}, \ \ \tilde{\lambda}_S = \frac{\lambda_S}{\lambda_0}, \ \ \tilde{c}_S = \frac{C_S}{c_p},$$

$$\mathrm{Ma}^{-2} = \frac{\gamma_{air} p_0}{\rho_0 u_0^2}, \ \ \mathrm{Re} = \frac{l_0^2}{t_0 \nu_{air}}, \ \ \mathrm{R}_{solid} = p_0 \left(\zeta_p \mu_{S0} \right)^{-1},$$

$$\mathrm{Pe}_T = \frac{l_0^2 \rho_0 c_p}{t_0 \lambda_0}, \ \ \mathrm{Pe}_1 = \frac{l_0^2}{t_0 D_0}, \ \ \tilde{Q} = \frac{Q t_0 k}{\rho_0 C_{pg} T_0}, \ \ \tilde{k} = \frac{t_0 k}{\rho_0}, \ \ p_0 = \frac{\mathrm{R} \rho_0 T_0}{M_0}, \ \ \tilde{\sigma}_{tot} = \frac{\sigma_{tot}}{p_0},$$

$$\tilde{K} = \frac{K}{\mu_{S0}}, \ \ \tilde{\mu}_{solid} = \frac{\mu_{solid}}{\mu_{S0}}, \ \ \tilde{j} = \frac{j}{j_0}, \ \ j = \sigma E,$$

$$\mathrm{Pe}_{el} = \frac{l_0^2 \rho_{el} c_{p,el}}{t_0 \lambda_{el}}, \ \ R_{el} = \frac{j_0^2 t_0}{l_0^2 T_0 \rho_0 c_{p,el}}, \ \ \mathrm{Pe}_{gr} = \frac{l_0^2 \rho_{gr} c_{p,gr}}{t_0 \lambda_{gr}},$$

$$\tilde{\sigma}_{el} = \frac{\sigma_{el}}{\sigma_{el,0}}, \ \ \tilde{E}_{el} = \frac{E_{el}}{E_{el,0}}, \ \ \tilde{\varphi} = \frac{\varphi}{\varphi_0}, \ \ \tilde{\kappa}_0 = \frac{\kappa_0 t_0 A}{c_p \rho_0 V} \qquad (9)$$

Here $t_9 = 1 \div 10\,(\mathrm{s})$, $l_0 = 0.018\,(\mathrm{m})$, $A = l_0^2\,(\mathrm{m}^2)$, $V = l_0^3\,(\mathrm{m}^3)$, $c_p = C_{p,air} = 1114\,(\mathrm{J/kg/K})$, $\rho_0 = \rho_{air} = 0.4\,(\mathrm{kg \cdot m^{-3}})$, $\lambda_0 = \lambda_{air} = 0.06\,(\mathrm{W/m/K})$, $D_0 = 2 \times 10^{-5}\,(\mathrm{m^2/s})$, $\mu_{S0} = 2 \times 10^9\,(\mathrm{Pa})$, $\nu_{air} = 9.7 \times 10^{-5}\,(\mathrm{m^2/s})$, $\lambda_{el} = 178\,(\mathrm{W \cdot m^{-1} \cdot K^{-1}})$, $\mathrm{Pe}_{el} = 0.000945$, $j_0 = 3500\,(\mathrm{A})$, $\mathrm{Pe}_{gr} = 3.132$, $\rho_{el} = 1.93 \times 10^4\,(\mathrm{kg \cdot m^{-3}})$, $c_{p,el} = 24.27\,(\mathrm{J \cdot mol^{-1} \cdot K^{-1}})$, $E_{el,0} = 100\,(\mathrm{V \cdot m^{-1}})$, $\varphi_0 = l_0 E_{el,0}\,(\mathrm{V})$, $\sigma_{el,0} = j_0 / E_{el,0}\,(\mathrm{m^{-1} \cdot Om^{-1}})$, $R_{el} = 2 \times 10^{-7} \div 2 \times 10^{-5}\,(\mathrm{m \cdot Om})$, $j_0 = 3500\,(\mathrm{A})$.

Densities of the components of the gas and solid phases are $\rho_{1g} = \rho_{N_2}$, $\rho_{1s} = \rho_{Zr}$, $\rho_{2s} = \rho_{ZrN}$. Temperature of gas and a mixture of solid components is T_g, T_S. Temperature of the graphite shell of the tungsten channel is T_{gr}, T_{el}. The temperature is found by the formula

$$T_{ge} = T_0 \left(1 + \beta \tilde{T}_{gr} \right), \ \ T_{el} = T_0 \left(1 + \beta \tilde{T}_{el} \right), \ \ T_g = T_0 \left(1 + \beta \tilde{T}_g \right), \ \ T_S = T_0 \left(1 + \beta \tilde{T}_S \right)$$

The value $\beta = RT_0 / E_{comb}$ is dimensionless parameter characterizing activation energy of combustion E_{comb}, $\beta_{pl} = RT_0 / E_{pl}$ dimensionless parameter characterizing activation energy of plasticity, $\beta = 0.084$, $\beta_{pl} = 0.05$. The values R, E, Q are the gas constant, the activation energy, the thermal effect of combustion; $p = \rho_g T_0 \left(1 + \beta \tilde{T}_g \right)$ is the gas pressure; κ_0 is dimensionless heat transfer coefficient; $\tilde{c}_S, \tilde{c}_{pg}$ is the heat capacity; $\tilde{\lambda}_S, \tilde{\lambda}_g$ is the thermal conductivity; the $\tilde{D}$ is diffusion coefficient; Ma, Re are the Mach and Reynolds numbers; $\mathrm{Pe}_T, \mathrm{Pe}_1$ are the thermal and diffusion Peclet numbers, the index refers to the parameters for air under normal conditions.

Let us present the basic equations in a form that admits a regular passage to the limit $\chi \to 0$ and $\chi \to 1$. The system of equations is presented below in dimensionless variables, the tilde symbol is omitted.

The equations of conservation of the phase density

$$\frac{\partial \chi \rho_g}{\partial t} + \nabla \cdot (\chi \rho_g \, \mathbf{u}) = -J_{g \to S}, \quad \frac{\partial (1-\chi) \rho_S}{\partial t} = J_{g \to S}, \quad J_{g \to S} = \frac{M_{1g}}{M_{1S}} J_{1S} \quad (10)$$

Mass conservation equation for nitrogen component N_2

$$\frac{\partial \chi \rho_g}{\partial t} + \nabla \cdot (\chi \rho_g \mathbf{u}) = -\frac{M_{1g}}{M_{1S}} J_{1S}, \quad \rho_{N2} = \rho_g \quad (11)$$

In reactions for the components of the solid phase, the reactants do not mix at the molecular level, diffuse and move within the solid phase. Mass conservation equation for solid phase can be written in the form

$$\frac{\partial (1-\chi) \rho_{1S}}{\partial t} = -J_{1S}, \quad \frac{\partial (1-\chi) \rho_{2S}}{\partial t} = \frac{M_{2S}}{M_{1S}} J_{1S}, \quad (12)$$

where mass flux for reaction (1) is $J_{1S} = \chi^2 (1-\chi) \left(\dfrac{\rho_{1g}}{M_{1g}} \right)^2 \dfrac{\rho_{1S}}{M_{1S}} k_1 \exp\left(\dfrac{T_g}{\beta T_g + 1} \right)$.

The equation of gas motion in pores [18−20] is as follows:

$$\frac{\partial \chi \rho_g \mathbf{u}}{\partial t} + \nabla \cdot (\chi \rho_g \, \mathbf{u}\mathbf{u}) + \mathrm{Ma}^{-2} \nabla p = \mathrm{Re}^{-1} \nabla \cdot \boldsymbol{\tau} + \mathbf{S_V}, \quad \boldsymbol{\tau} = \mu \left[\nabla \mathbf{u} + (\nabla \mathbf{u})^T - \frac{2}{3} (\nabla \cdot \mathbf{u}) \mathbf{I} \right], \quad (13)$$

where the term $\mathbf{S_V}$ of the distributed gas resistance in the pores has the form $(\mathbf{S_V})_j = -u_j \eta_j$, $\eta_j = \eta_{1j} |\mathbf{u}| + \eta_{0j}$, u_j are the velocity components in the Cartesian coordinate system. $p = \rho_g (1 + \beta T_g)$ is the gas phase pressure.

Let us write down the equation of the solid motion phase in the simplest case, neglecting the influence of the work of mechanical stresses on the temperature field [34]

$$\frac{\partial (1-\chi) \rho_S \, \mathrm{V}_{solid}}{\partial t} + \nabla \cdot [(1-\chi) \rho_S \, \mathrm{V}_{solid} \mathrm{V}_{solid}] = \mathrm{R}_{solid}^{-1} \nabla \cdot \sigma,$$

$$\sigma_{ij} = 2 \mu_{S1} \varepsilon_{ij} + \delta_{ij} \left(\mu_{S2} \sum_k \varepsilon_{kk} - K \omega \right), \quad (14)$$

where R_{solid} is the Reynolds number of the solid phase.

The heat balance equation for the gas phase, including dispersion, is written in the form

$$\rho_g c_{pg} \chi \left(\frac{\partial T_g}{\partial t} + \mathbf{u} \cdot \nabla T_g \right) + c_g T_g \chi J_{S \to g} = \nabla \cdot \left(\chi \frac{\mathrm{D}_{Tg}}{\mathrm{Pe}_{Tg}} \nabla T_g \right) - \kappa \chi (1-\chi) (T_g - T_S) + \chi Q_r \quad (15)$$

The heat flux of chemical transformation

$$Q_r = Q_r^0 \chi^2 (1-\chi) \left(\frac{\rho_{1g}}{M_{1g}} \right)^2 k_1 \exp\left(\frac{T_g}{\beta T_g + 1} \right)$$

is included in the right side of the equation. The thermal dispersion tensor [22] takes into account the longitudinal and transverse dispersion

$$D_{Tg} = \begin{pmatrix} \lambda_{1g} & 0 \\ 0 & \lambda_{2g} \end{pmatrix}, \ \lambda_{1g} = \lambda_g \left[\xi + \varphi_1 \left(Pe_{1t} \right) \right], \ \lambda_{2g} = \lambda_g \left[\xi + \varphi_2 \left(Pe_{2t} \right) \right]$$

The heat balance equation for the solid phase has the form

$$\rho_S c_S (1-\chi) \left(\frac{\partial T_S}{\partial t} + V_{solid} \cdot \nabla T_S \right) = \nabla \cdot \left[(1-\chi) \frac{\lambda_S}{Pe_{Ts}} \nabla T_S \right] + \kappa \chi (1-\chi)(T_g - T_S) + (1-\chi) Q_r \quad (16)$$

The heat transfer coefficient between the gas and solid phases is described using the Leveque formula [19, 51] in the form $\kappa = \kappa_0 \left(1 + Re_{loc}^{0.3} Pe_{Tloc}^{0.3} \right)$. Here $Re_{loc} = Re |\mathbf{u}| \rho_g$, $Pe_{Tloc} = Pe_{Tg} |\mathbf{u}| \rho_g$ are the local Reynolds and Peclet numbers [19], (velocity and density are dimensionless!) $Re_{loc} = Re |\tilde{\mathbf{u}}| \tilde{\rho}_g$, $Pe_{Tloc} = Pe_{Tg} |\tilde{\mathbf{u}}| \tilde{\rho}_g$.

Equation of heat balance in a graphite shell is

$$\rho_{gr} c_{gr} \left(\frac{\partial T_{gr}}{\partial t} \right) = \nabla \cdot \left(\frac{\lambda_{gr}}{Pe_{gr}} \nabla T_{gr} \right) \quad (17)$$

Equation of heat balance in a tungsten channel is

$$\rho_{Wr} c_{Wr} \left(\frac{\partial T_{Wr}}{\partial t} \right) = \nabla \cdot \left(\frac{\lambda_{Wr}}{Pe_{Wr}} \nabla T_{Wr} \right) + Q_{Joul} \quad (18)$$

E-field equations based on the Ohm's law are

$$\nabla \cdot \nabla \varphi = 0, \ j = \sigma E, \ j = -\sigma \nabla \varphi, \ E = -\nabla \varphi \quad (19)$$
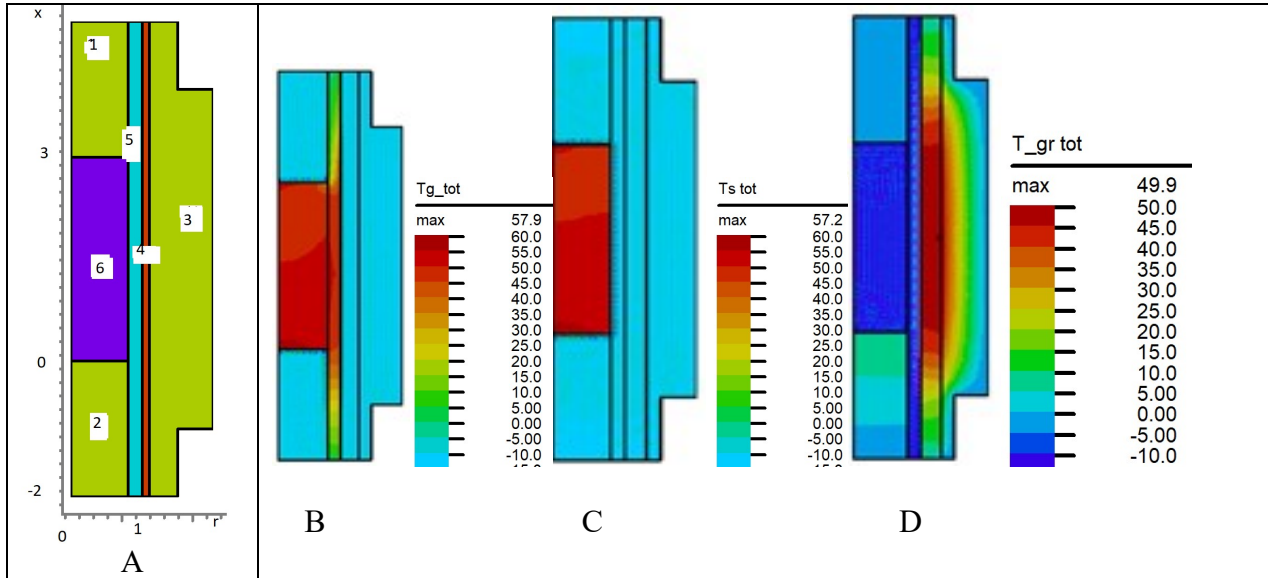

Fig. 1. Schematic of the SPS reactor (fig. 1, A). The modeling area is shown, consisting of zones 1−6. Zone 1: $3 < x < 5$, $0 < r < R_1$. Zone 2: $-2 < x < 0$, $0 < r < R_1$. Zone 3: $-1 < x < 4$, $1 + \delta < r < R_2$ - graphite reactor vessel. Zone 4: $-2 < x < 5$, $1 < r < 1 + \delta$ − tungsten layer. Zone 5: $0 < x < 3$, $R_1 < r < 1$ − feed channel of N₂. Zone 6: $0 < x < 3$, $0 < r < R_1$ − porous area of a mixture of reagents and synthesis products. Fig. 1, B and Fig. 1, C illustrates the temperature distribution of the gas and the solid phase in zone 6 at time instance $t = 0.88$. Fig. 1, D shows the temperature distribution of a graphite body in zones 1, 2, 3 at time instance $t = 0.88$ using a tungsten layer $-2 < x < 5$, $1 < r < 1.2$

Boundary and initial conditions. The relations are prescribed for the reactor consisting of zones 1−6 that are as follows: the graphite body is presented by zones 1, 2, 3; the tungsten alloy of combustion initiation is shown by zone 4; the channel of N_2 supply is shown by zone 5; and the porous region of synthesis consisted of species N_2, Zr, and ZrN is presented by zone 6 (see fig. 1, A).

Boundary conditions at the graphite body (zones 1, 2, 3).

At $x = -2$, $0 < r < 1 - d$; $x = 5$, $0 < r < 1 - d$; $-2 < x < 5$, $r = 1 + \delta$; and outer boundary of zone 3 the boundary conditions are as follows

$$\frac{\partial T_{gr}}{\partial n} = \alpha_{ex}\left(T_{ex} - T_{gr}\right), \text{ at } -2 < x < 0, \, r = 1 - d \qquad (20)$$

At $x = -2$, $0 < r < 1 - d$; $3 < x < 5$, $r = 1 - d$ the thermal radiation/absorption condition was set according to the Stefan − Boltzmann law are imposed which in dimensionless variables has the form

$$\frac{\partial T_g}{\partial n} = -q_{g,rad}, \quad \frac{\partial T_S}{\partial n} = -q_{S,rad},$$

$$q_{g,rad} = \varepsilon_\Sigma \frac{A_W}{\beta}\left[\left(1 + \beta T_W\right)^4 - \left(1 + \beta T_g\right)^4\right], \quad q_{S,rad} = \varepsilon_\Sigma \frac{A_W}{\beta}\left[\left(1 + \beta T_W\right)^4 - \left(1 + \beta T_{gr}\right)^4\right], \quad (21)$$

where T_{gr} is the temperature of the graphite body at the inner boundary between zones 3, 4; A_W is the Boltzmann's constant in dimensionless variables

$$A_W = \frac{2\chi l_0^2}{r_p} \frac{\sigma_B}{\lambda_0} T_0^3, \, [52].$$

On the inner boundary between zones 4, 5 $-2 < x < 5$, $r = 1 + \delta$ the boundary condition has the form

$$\frac{\partial T_{gr}}{\partial n} = -q_{gr,rad}, \quad q_{gr,rad} = \varepsilon_\Sigma \frac{A_W}{\beta}\left[\left(1 + \beta T_{el}\right)^4 - \left(1 + \beta T_{gr}\right)^4\right] \qquad (22)$$

On the boundary of zone 4 (tungsten alloy), an electric field potential $\varphi(t)$ is set, which depends on time, which makes it possible to generate electric $E(t)$ and electric current $j(t)$ and control the initiation of combustion and the thermal regime of densification of zirconium nitride.

On the inner boundary between zones 4, 5 $-2 < x < 5$, $r = 1 + \delta$ the boundary condition has the form

$$\frac{\partial T_g}{\partial n} = -q_{g,rad}, \quad q_{g,rad} = \varepsilon_\Sigma \frac{A_W}{\beta}\left[\left(1 + \beta T_{el}\right)^4 - \left(1 + \beta T_g\right)^4\right] \qquad (23)$$

Boundary conditions at the entrance to the reactor zone 5 $x = -2$, $1 - d < r < 1$ are

$$u = u_{in}, v = 0, \, p = p_{in}, \quad \frac{\partial T_g}{\partial n} = -q_f(t), \quad \frac{\partial \rho_g}{\partial n} = -N_{2f} \qquad (24)$$

Boundary conditions at the exit from the reactor zone 5 read

$$t > 0; \, x = 5; 1 - d < r < 1 : \frac{\partial u}{\partial x} = 0, v = 0, \, p = p_{ex},$$

$$\frac{\partial T_g}{\partial n} = \alpha_{ex}\left(T_{ex} - T_g\right), \frac{\partial T_S}{\partial n} = \alpha_{ex}\left(T_{ex} - T_S\right) \qquad (25)$$

On the inner boundaries of the zone 5 $-2 < x < 0$, $r = 1-d$, and $-1 < x < 4$, $r = 1$ the boundary condition has the form

$$\frac{\partial T_g}{\partial n} = -q_{g,rad}, \quad \frac{\partial T_S}{\partial n} = -q_{S,rad}, \quad q_{g,rad} = \varepsilon_\Sigma \frac{A_W}{\beta}\left[(1+\beta T_W)^4 - (1+\beta T_g)^4\right] \tag{26}$$

Boundary conditions for zones 1, 2, 6 on the axis of symmetry of the reactor $-2 < x < 5$, $r = 0$ have the form

$$t > 0, \ r = 0: \ v = 0, \ \frac{\partial T_g}{\partial n} = 0, \ \frac{\partial T_S}{\partial n} = 0, \ \frac{\partial T_{gr}}{\partial n} = 0 \tag{27}$$

The condition $T_S = T_g$ at the inner boundary between the channel and zone 6, $0 < x < 3$, $r = 1-d$ if imposed, $\partial/\partial n$ denotes the normal derivative, $R_1 = 1-d$.

Initial conditions.

$$t = 0, \ u = 0, \ v = 0, \ T_g = T^0, \ T_S = T^0, \ T_{gr} = T^0, \ T_{el} = T^0, \ T_g = T^0, \ T_S = T^0,$$

$$t = 0; \ 0 < x < 3; \ 0 < r < 1-d: \ u = u^0, \ v = 0, \ \rho_g = \rho_g^0, \ \rho_{jS} = \rho_{jS}^0, \ j = 1,2, \tag{28}$$

where the superscript zero refers to the value of the variable at the initial time.

The finite element method tested in our previous papers [10−23] has been applied. The results of simulation were validated using various meshes. The results of numerical solution of equations (10)−(19) with relations (6)−(8), (20)−(28) are presented in fig. 1, B, fig. 1, C, fig. 1, D, fig. 2−fig. 10.

The satisfactory agreement of porosity calculation with experiment [16] is demonstrated in fig. 2 for $r_p = 1.2 \times 10^{-5}$, $m = 0.33$, $A_0 = 4.3 \times 10^{-9}\left(\text{Pa} \cdot \text{s} \cdot \text{K}^{-1}\right)$ and $r_p = 8.5 \times 10^{-6}$, $m = 0.36$, $A_0 = 5.4 \times 10^{-9}\left(\text{Pa} \cdot \text{s} \cdot \text{K}^{-1}\right)$, see formula (8) for temperature rise with rate 10 C/min. Symbols 1 refer to SPS, $T = 1100(\text{C})$, fig. 2, A and SPS, $T = 1200(\text{C})$, fig. 2, B respectively, $t_9 = 10(\text{s})$.
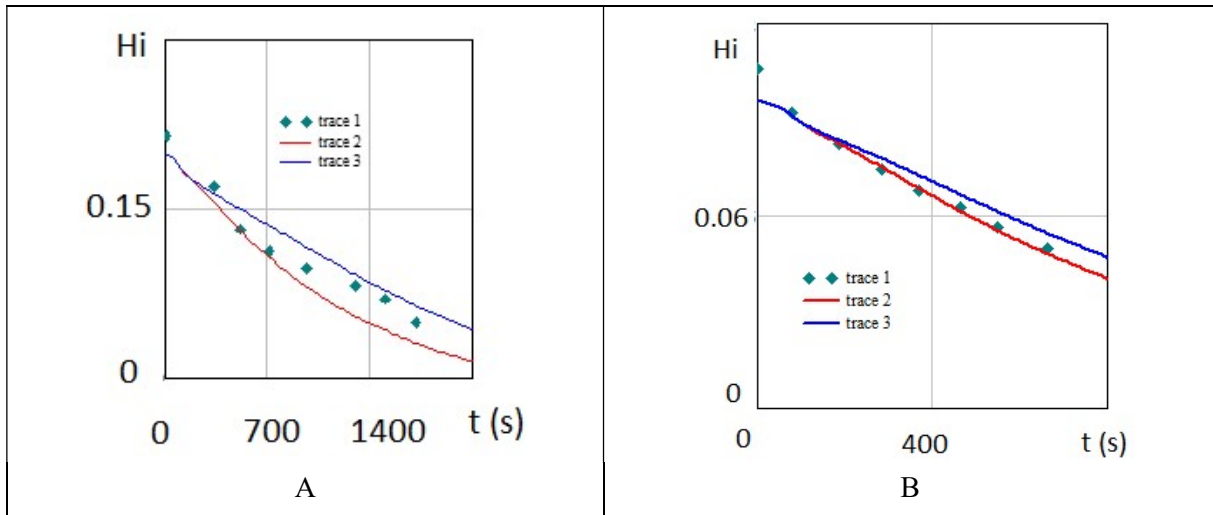

Fig. 2. The comparison with experiment. The comparison of porosity with experiment [16] for $r_p = 1.2 \times 10^{-5}$, $m = 0.33$, $A_0 = 4.3 \times 10^{-9}\left(\text{Pa} \cdot \text{s} \cdot \text{K}^{-1}\right)$ and $r_p = 8.5 \times 10^{-6}$, $m = 0.36$, $A_0 = 5.4 \times 10^{-9}\left(\text{Pa} \cdot \text{s} \cdot \text{K}^{-1}\right)$, see formula (8) is shown in fig. 2, B for temperature rise with rate 10 C/min. Symbols 1 refer to SPS, $T = 1100(\text{C})$, fig. 2, A and SPS, $T = 1200(\text{C})$, fig. 2, B respectively, $t_9 = 10(\text{s})$. Solid lines 2, 3 in fig. 2, A refer to porosity at points with coordinates $(0.9, 0.5)$, $(1.42, 0.5)$ and lines 2, 3 in fig. 2, B refer to porosity at points with coordinates $(0.9, 0.75)$, $(2.14, 0.75)$

The change in gas temperature in fig. 3, B and solid phase temperatures in fig. 3, D demonstrates the dynamics of heating and the degree of nonequilibrium, which follows from the difference between T_g and T_s near the boundary $0 < x < 3$, $r = 0.8$.

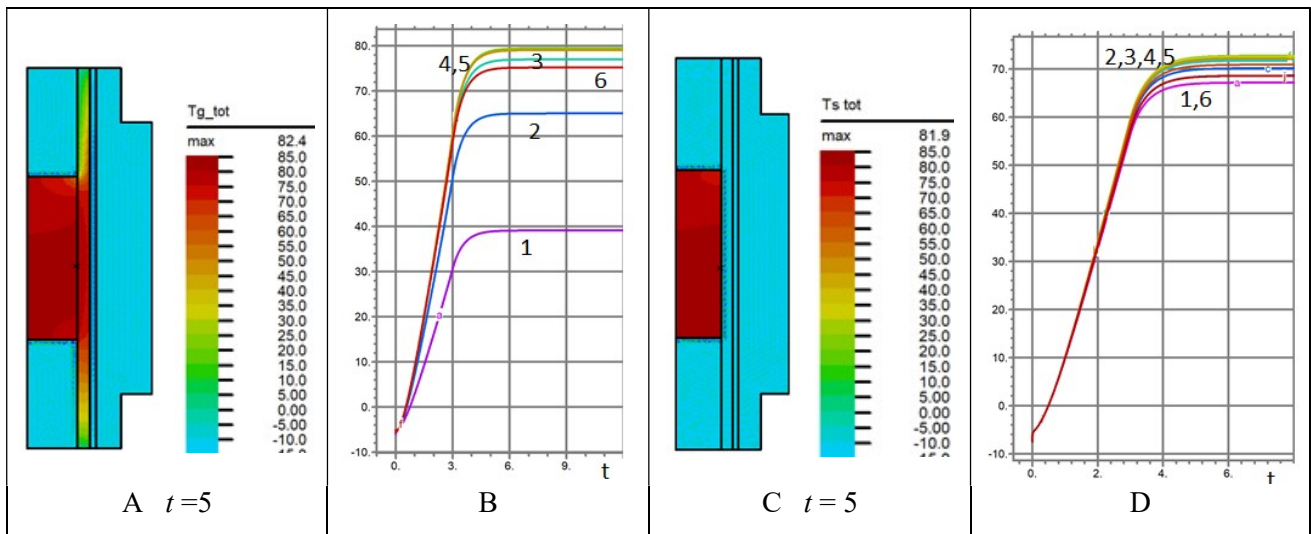A $t = 5$ B   C $t = 5$ D

Fig. 3. The gas temperature (fig. 3, A, fig. 3, B) and the temperature of the solid phase (fig. 3, C, fig. 3, D). In fig. 3, A, fig. 3, C illustrates the field T_g (t,x,r), T_s (t,x,r) $t = 5$; fig. 3, B, fig. 3, D illustrates the T_g and T_s dynamics. Lines 1−6 refer to points (x,r) with coordinates: (0, 0.75), (0.14, 0.75), (0.9, 0.75), (1.42, 0.75), (2.14, 0.75), (2.86, 0.75) respectively

The dynamics of the synthesis of zirconium nitride shown in fig. 4, A, fig. 4, B, fig. 4, C, demonstrates the degree of inhomogeneity of the $ZrN(t,x,r)$ distribution at $t = 4$ and $t = 5$. By the time $t = 20$, the distribution of $ZrN(t,x,r)$ is close to uniform, with the porosity $\chi_{ex} = 5 \times 10^{-4}$ of the graphite body.

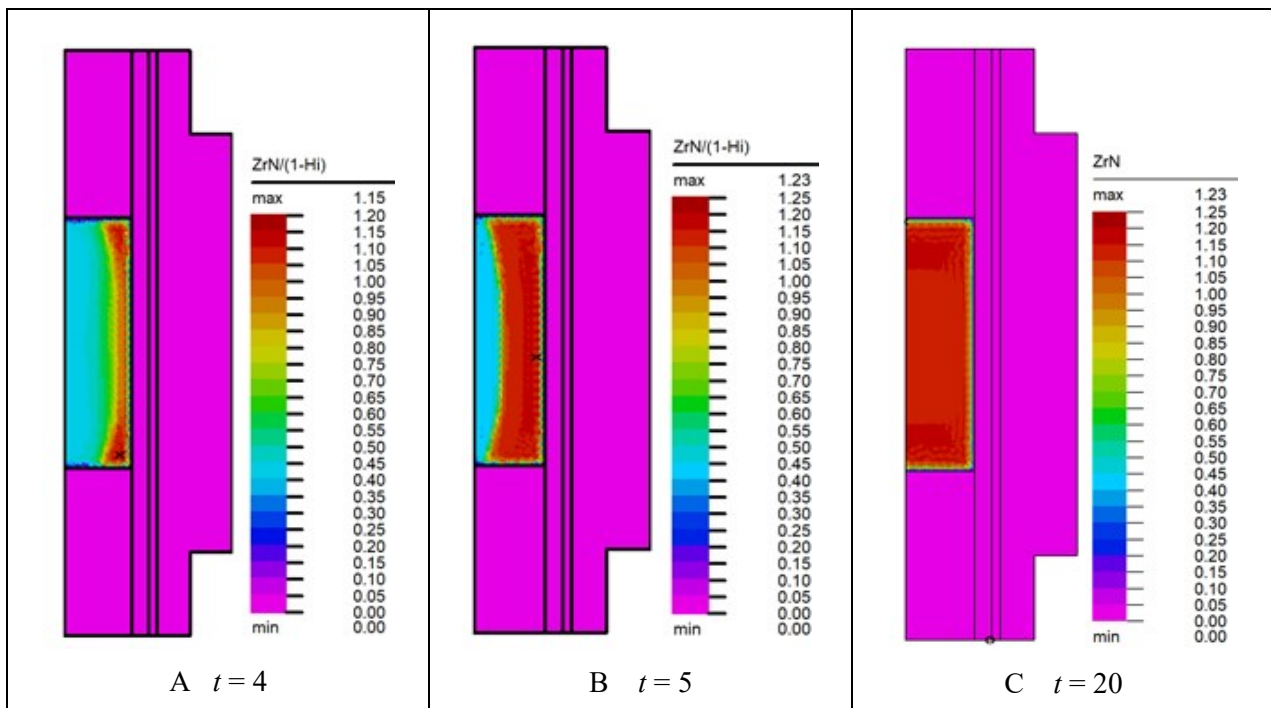
A $t = 4$ B $t = 5$ C $t = 20$

Fig. 4. The dynamics of the synthesis of zirconium nitride is illustrated. Fig. 4, A, fig. 4, B and fig. 4, C shows the field $ZrN(t,x,r)$ at time instances $t = 4$, $t = 5$, and $t = 20$, respectively

Figure 5 shows the effect of the two-stage nitrogen supply at time intervals: $N_{2f} = 1$, $0 < t < 0.2$ and $N_{2f} = 0$, $0.2 < t < 5$, and $t > 10$. The time history of the density N_2 at points with coordinates (1/7, 0.5), (5/77, 0.5), (10/7, 0.5), (15/7, 0.5), (20/7, 0.5) is shown in fig. 5A. Note the deficit of the reagent N_2 in the time interval 0, $0.2 < t < 5$, leading to a zone of constant distribution of Zr and ZrN densities lines 3, 4, 5 in fig. 5, B and fig. 5, C.
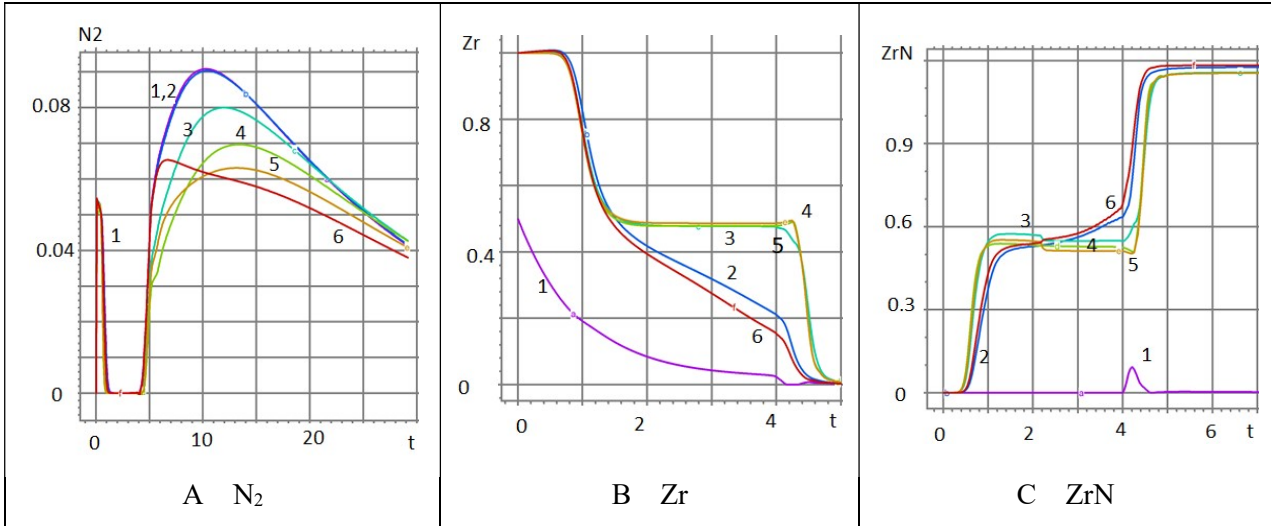

Fig. 5. The dynamics of nitrogen, zirconium and zirconium nitride in a two-stage nitrogen supply mode is illustrated. The fig. 5, A, fig. 5, B and fig. 5, C shows the time variation of N_2, Zr and ZrN, respectively, at points with coordinates (0, 0.5), (0.14, 0.5), (0.9, 0.5), (1.42, 0.5), (2.14, 0.5), (2.86, 0.5)

Figure 6 presents the field of activation energy $A_m(t,x,r)$ at time instance $t = 10$ (fig. 6, A) and the time history of $A_m(t,x,r)$ at points with coordinates (0, 0.8), (0.14, 0.8), (0.9, 0.8), (1.42, 0.8), (2.14, 0.8), (2.86, 0.8), lines 1−6 respectively (fig. 6, B). The activation energy $A_m(t,x,r)$ is applied for the densification process using the Olevsky model.
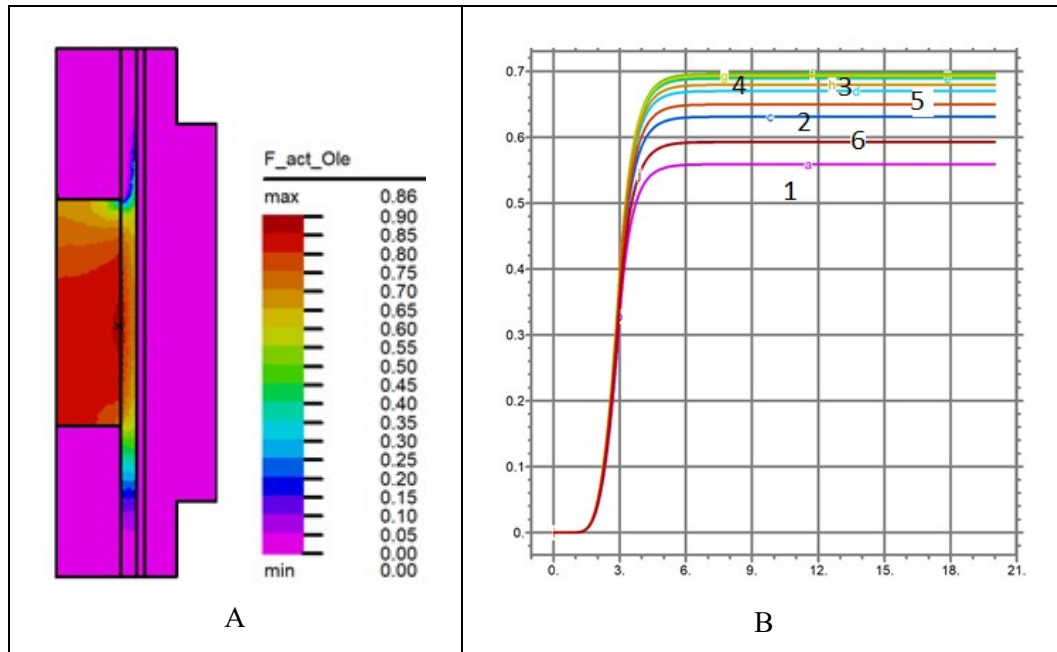

Fig. 6. The activation energy $A_m(t,x,r)$ of the densification process in the Olevsky model. The field $A_m(t,x,r)$ is shown in fig. 6, A, at time instance $t = 10$. The time history of $A_m(t,x,r)$ at points with coordinates (0, 0.8), (0.14, 0.8), (0.9, 0.8), (1.42, 0.8), (2.14, 0.8), (2.86, 0.8), lines 1−6 respectively is shown in fig. 6, B

Figure 7 shows the densification process in the time interval $0 < t < 20$, fig. 7, B and fig. 7, C. Figure 7, A shows the ratio of the porosity at time to the initial porosity $\lg(\chi(t,x,r)/\chi_0)$. The porosity of the solid phase during densification was calculated according to the formulas (2) and (5). Figure 7, A $\chi(t,x,r)/\chi_0$ at time instance $t = 40$. The rime history $\lg(\chi(t,x,r)/\chi_0)$ at points with coordinates (0, 0.75), (0.14, 0.75), (0.9, 0.75), (1.42, 0.75), (2.14, 0.75), (2.86, 0.75) for $\chi_{ex} = 5 \times 10^{-4}$ is presented in fig. 7, B and fig. 7, C. Note the value $\chi(t,x,r)/\chi_0$ are three orders of magnitude, lines 3, 4, 5 in fig. 7, B and fig. 7, C. Slower densification occurs near the boundary of the synthesis zone with graphite whose porosity is $\chi_{ex} = 5 \times 10^{-4}$ see fig. 7, A and lines 1−6 in fig. 7B and fig. 7, C.
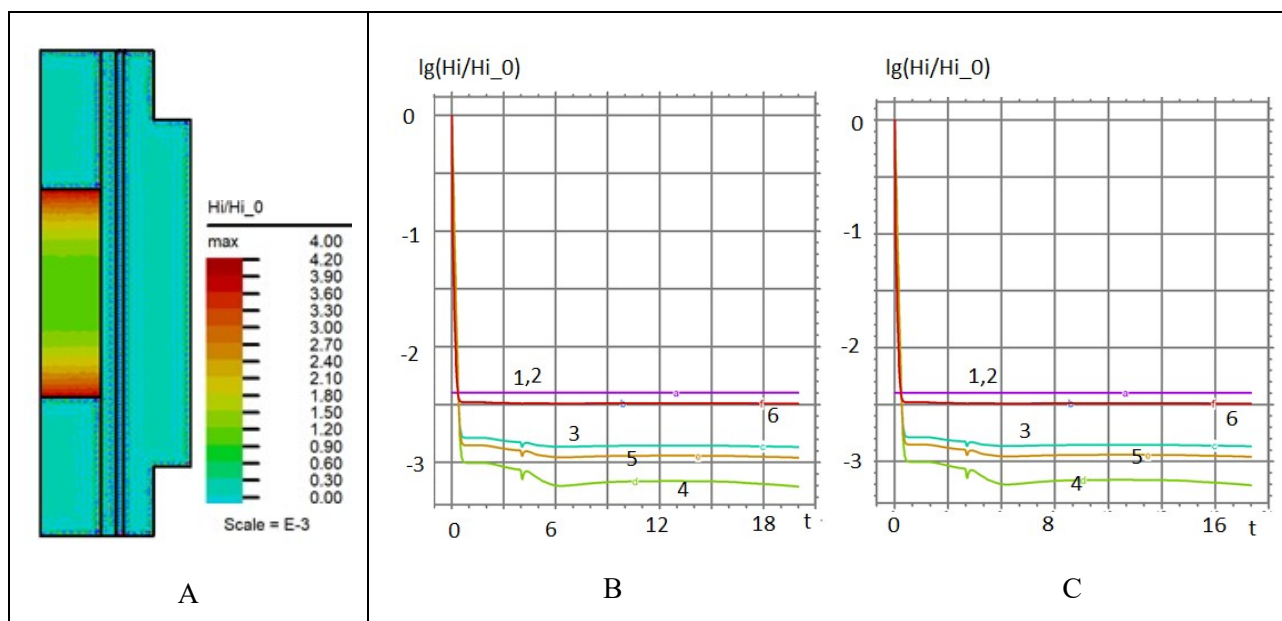

Fig. 7. The porosity of the solid phase $r_p = 5 \times 10^{-7}$ in the densification process is shown according to the formulas (2) and (5). In fig. 7, A, the $\chi(t,x,r)/\chi_0$ ratio of the porosity at the time instance t to the initial porosity is given. In fig. 7, B and fig. 7, C shows the change in time of the decimal logarithm $\lg(\chi(t,x,r)/\chi_0)$ at points with coordinates (0, 0.75), (0.14, 0.75), (0.9, 0.75), (1.42, 0.75), (2.14, 0.75), (2.86, 0.75) and (0, 0.) (0.14, 0.), (0.9, 0.), (1.42, 0.), (2.14, 0.), (2.86, 0.) respectively

Figure 8 shows the dynamics $i_{elast}(t,x,r)$ for $\chi_{ex} = 10^{-3}$. Note the expansion of the zone of $i_{elast}(t,x,r) = 0$ thermoplastic properties of ZrN in the middle of the synthesis region and a decrease in the size of the zone $i_{elast}(t,x,r) = 1$ in which the thermoelastic properties of ZrN are manifested at moments. time $t = 1.43$, $t = 1.55$, $t = 1.64$ and $t = 20$ in fig. 8, A, fig. 8, B, fig. 8, C and fig. 8, D.

As you can see from fig. 9, A, by the time $t = 40$, the region of thermoplastic change in the solid phase prevails in the reactor. The thermoelastic properties of the solid phase, which at this time is almost entirely composed of zirconium nitride, appear in the regions near the boundaries of the reactor: $x = 0, 0 < r < 0.8$ and $x = 3, 0 < r < 0.8$ (see fig. 1, A). Tracing the dynamics $i_{elast}(t,x,r)$ for $\chi_{ex} = 5 \times 10^{-4}$ at points with coordinates: (5/7.0), (10/7.0), (15/7.0), (20/7.0), lines 2−6, shown in fig. 9, B, we note that having arisen at points in time with a zero ordinate of points on lines 2−6, the thermoplastic properties of ZrN change to thermoelastic properties, and these properties are inherent in ZrN at all subsequent moments. time $t < 21$. Note the difference in the dynamics of the thermoplastic and thermoelastic properties of ZrN in the case of the higher porosity of the graphite shell, fig. 9, C. The difference from the case considered above is that, having arisen at times with a zero ordinate of points on lines 2−6, the thermoplastic properties of ZrN change to thermoelastic properties, which are again replaced by thermoplastic ones at $t > 18$.
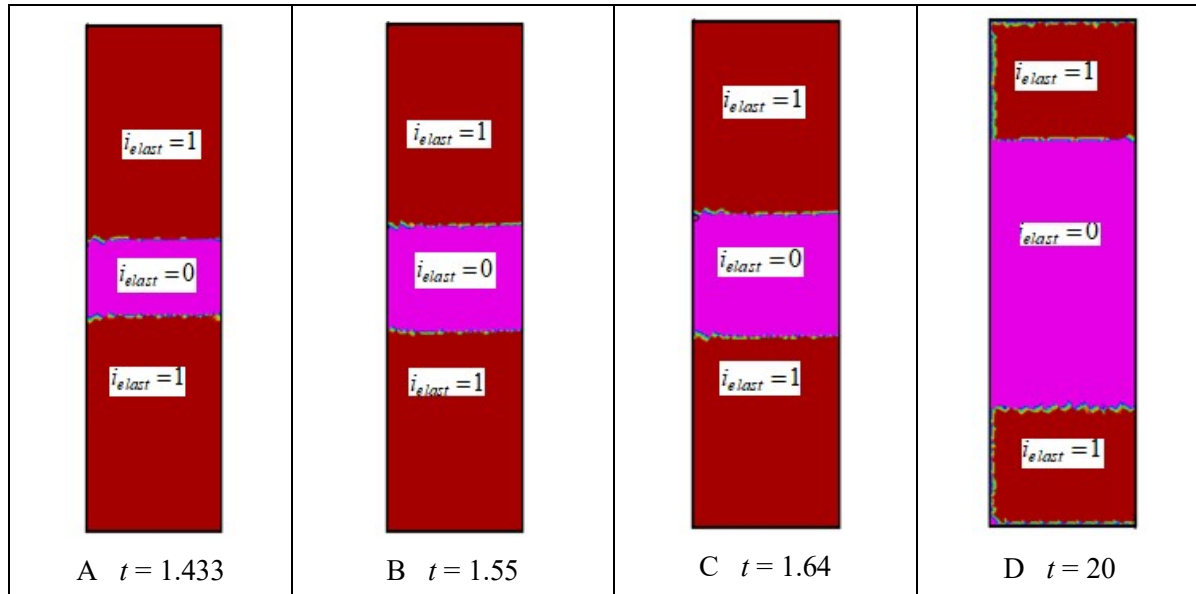
Fig. 8. The dynamics of the zones of densification are illustrated by the thermoelasticity model $i_{elast}(t,x,r)=1$ and the thermoplasticity mode $i_{elast}(t,x,r)=0$. In fig. 8, A, fig. 8, B, fig. 8, C and fig. 8, D shows the zones at times $t=1.43$, $t=1.55$, $t=1.64$ and $t=20$, respectively
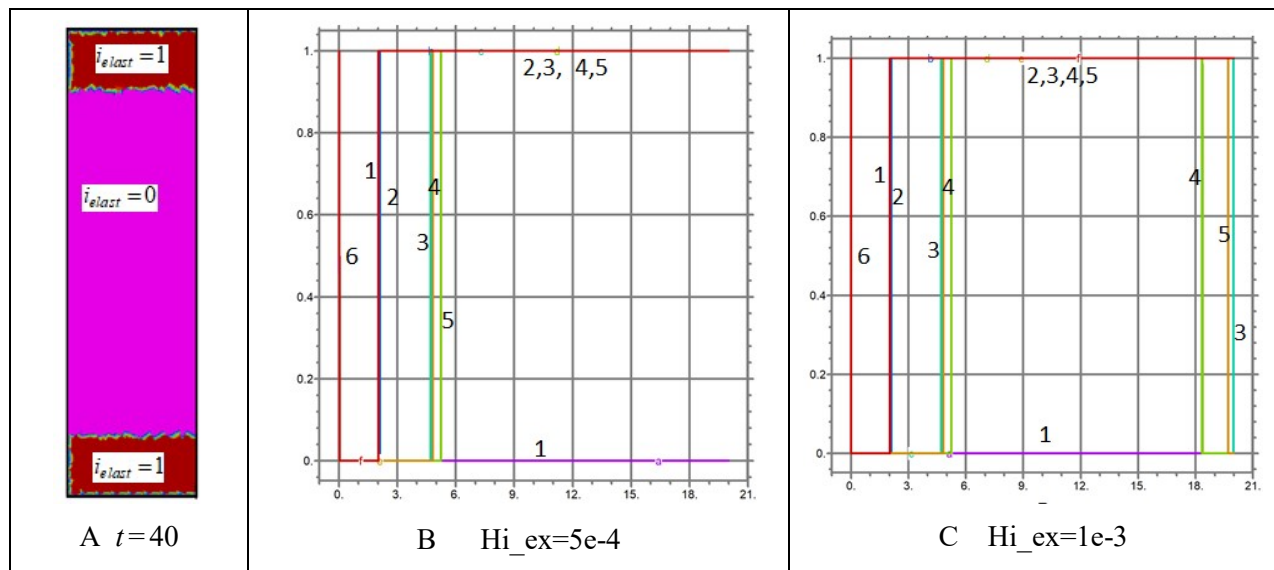

Fig. 9. The zones of densification $i_{elast}(t,x,r)=1$ are given according to the thermoelasticity model and the thermoplasticity mode $i_{elast}(t,x,r)=0$ for external porosity $\chi_{ex}=5\times10^{-4}$ and $\chi_{ex}=10^{-3}$. Fig. 9, A shows the zones at times $t=40$, $\chi_{ex}=5\times10^{-4}$. Fig. 9, B, and fig. 9, C show the dynamics of the zones at $\chi_{ex}=5\times10^{-4}$ and $\chi_{ex}=10^{-3}$, respectively. The time history of the value $i_{elast}(t,x,r)=1$ at points with coordinates is illustrated: (0, 0.), (0.14, 0.), (0.9, 0.), (1.42, 0.), (2.14, 0.), (2.86, 0.), lines 1−6, respectively

The heating of the graphite shell at a given increase in the electric field strength $E(t)=\sqrt{0.5\cdot t}$, $0<t<34$ and $E(t)=0$, $t\geq4$ is presented by the temperature distributions T_gr (t, x, r) at times $t=1$, $t=3$ and $t=5$ in fig. 10, A, fig. 10, B and fig. 10, C respectively. Note the maximum values of T_gr = 4, 22, and 42 at times $t=1$, $t=3$, and $t=5$.
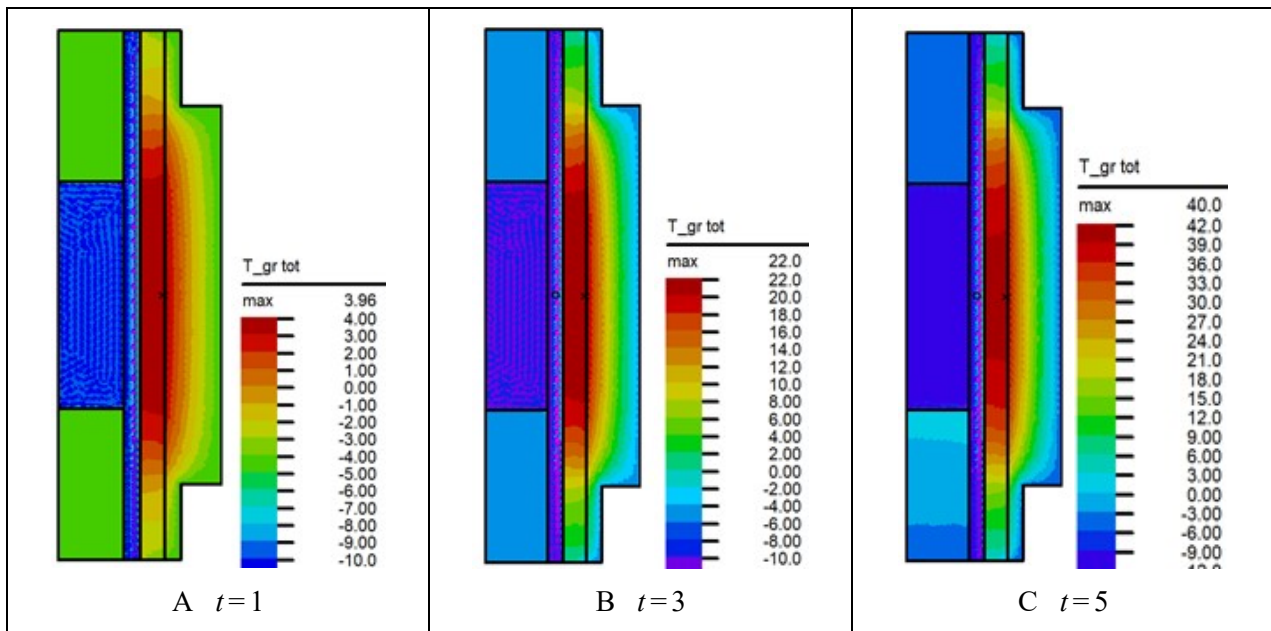
17

Fig. 10. Dynamics of heating the graphite body for the thickness of region 5 (fig. 1) Delta_r = 0.3. In fig. 10, A, fig. 10, B and fig. 10, C shows the T_gr (t, x, r) field at times $t = 1$, $t = 3$, and $t = 5$, respectively

Conclusion

The investigation of the synthesis and densification of zirconium nitride was carried out in the proposed model of multitemperature reactor, which differs from the typical model of the SPS reactor [38−40] by the presence of a gas flow channel and an electrically conductive tungsten alloy layer. The study of volumetric changes and variable porosity during the concentration expansion of the solid phase in the synthesis of zirconium nitride in a two-stage that consist of synthesis and sintering processes was carried out. A generalization of the two-temperature model [33, 37] and a variable porosity formula are proposed for self-consistent calculation of the multitemperature heat transfer. The computation including thermal radiation, concentration expansion, thermal and mass dispersion are presented The coefficients of concentration expansion are found in the process of zirconium combustion in the porous zone of the reactor, depending on the kinetics of synthesis of zirconium nitride at given initial values of gas and solid phases for unsteady nitrogen supply through gas channel. The approach allows us to control the rate of nitrating.

The effect of electric current on spark plasma densification and sintering (SPS) of ZrN powder was investigated. The thermoplasticity equation [38] was applied, taking into account the effect of electric current and generalization of the porosity formula [33] for calculating the thermoelastic properties of the solid phase during the synthesis and densification of ZrN. The temperature inside the mixture of zirconium powder with synthesized zirconium nitride, the temperature of the gas phase (N_2) and the temperature of the porous graphite shell of the reactor at a given electric potential applied to the electrodes of the tungsten layer and a given variation in time the electric current density is simulated. A model of the elastic limit for a porous mixture of solid particles with a gas phase is proposed, using the elastic limit for a solid spherical particle, the particle size and the number particle density. Calculations of the densification of zirconium nitride with the separation of zones in which the thermoelastic and thermoplastic properties of the solid phase prevail for the average particle size of 5e-7 have been carried out. A decrease in porosity by three orders of magnitude compared to the value is demonstrated. The influence of the low porosity of the graphite shell of the SPS reactor on the dynamics of densification is considered.

Estimation of volumetric deformations. arising as a result of a change in the temperature and concentration of a mixture of reagents and a product of ZrN during synthesis were caried out. The controlled Joule heating by electric current in a conducting layer, allows to conclude that the tem-

perature change during synthesis and densification depends significantly on the initial phase composition and effects the final ZrN distribution in the sample, its volume as well as the duration of the process.

The performed modeling of the synthesis and densification of ZrN indicates an uneven distribution of thermoelastic, thermoplastic properties, and porosity of ZrN in the reactor. The results obtained demonstrate a significant effect of variable porosity on the synthesis of fine ZrN particles. The ZrN densification mechanism can be changed through enhanced movement of dislocations due to local resistive heating [1].

The developed model of the SPS reactor with a gas flow and an electrically conductive layer can be applied with the adjustment of parameters according to the data of experiments to simulate compacting mechanisms for other electrically conductive materials subjected to sintering using an electric field [1, 38].

Refferences

1. Harrison, R. W.& Lee, W. E., "Processing and properties of ZrC, ZrN and ZrCN ceramics," *Advances in Applied Ceramics*, Vol. 115, No. 5, 2016, pp. 294−307. doi: 10.1179/1743676115Y.0000000061

2. Munir, Z. A., Anselmi-Tamburini, U. and Ohyanagi, M., "The effect of electric field and pressure on the synthesis andconsolidation of materials: a review of the spark plasmasintering method," *J. Mater. Sci.*, Vol. 41, No. 3, 2006, pp. 763–777.

3. Hulbert, D. M., Anders, A., Andersson, J., Lavernia, E. J. and Mukherjee, A. K., "A discussion on the absence of plasma inspark plasma sintering," *Scr. Mater.*, Vol. 60, No. 10, 2009, pp. 835–838.

4. Jackson, H. F. and Lee, W. E., "Properties and characteristics of ZrC," in *Comprehensive nuclear materials*, (ed. R. J. M. Konings), pp. 339–372; 2012, Oxford, Elsevier.

5. Zhao, Shijiao, Ma, Jingtao, Xu, Rui, Lin, Xuping, Cheng, Xing, Hao, Shaochang, Zhao, Xingyu, Deng, Changsheng, Liu, Bing, "Synthesis and Characterization of Zirconium Nitride Nanopowders by Internal Gelation and Carbothermic Nitridation," *Scientific reports*, Vol. 9, No. 19199, 2019. https://doi.org/10.1038/s41598-019-55450-x

6. Dietz, A. A., *Oxynitride ceramic materials based on combustion products of industrial metal powders in air*, Dissertation, Tomsk, 2006.

7. Russias, J. Cardinal, S. Esnouf, C. Fantozzi, G., and Bienvenu, K., "Hot pressed titanium nitride obtained from SHS starting powders: influence of a pre-sintering heat-treatment of the starting powders on the densification process," *J. Eur. Ceram. Soc.*, Vol. 27, No. 1, 2007, pp. 327−335.

8. Sakai, T. and Iwata, M., "Effect of oxygen on sintering of AlN," *J. Mater. Sci.*, Vol. 12, No. 8, 1977, pp. 1659–1665.

9. Adachi, J., Kurosaki, K., Uno, M., and Yamanaka, S., "Thermal and electrical properties of zirconium nitride," *J. Alloys Compd.*, Vol. 399, No. 12, 2005, pp. 242–244.

10. Merja, P., Masahide, T., Tsuyoshi, N., "Sintering and characterization of (Pu,Zr)N," *J. Nucl. Mater.*, Vol. 444, 2014, pp. 421−427.

11. Samsonov, G. V., *Nitrides*, ed. E.E. Gritsenko, Kiev: Naukova Dumka, 1969, 379 p.

12. Kurganov, G. V., Levinsky, Yu. V., et al., *Chemistry and Physics of Nitrides*, Kiev: Naukova Dumka, 1968, 47 p.

13. Harrison, R., Rapaud, O., Pradeilles, N., Maitre, A., and Lee, W. E., "On the fabrication of ZrCxNy from ZrO$_2$ via two-step carbothermic reduction-nitridation," *J. Eur. Ceram. Soc.*, Vol. 35, No. 5, 2015, pp. 1413−1421.

14. Aigner, K., Lengauer, W., Rafaja, D., and Ettmayer, P., "Lattice parameters and thermal expansion of Ti(CxN^x), Zr(CxN^x), Hf(CxN1.x) and TiN^x from 298 to 1473 K as investigated by high-temperature X-ray diffraction," *J. Alloys Compd.,* Vol. 215, No. 1-2, 1994, pp. 121−126.

15. Lee, G., Yurlova, M. S., Giuntini, D., Grigoryev, E. G., Khasanov, O. L., McKittrick, J., Olevsky, E. A., "Densification of zirconium nitride by spark plasma sintering and high voltage electric discharge consolidation: A comparative analysis," *Ceram. Int*., Vol. 41, No. 10, Part B, 2015, pp. 14973−14987.

16. Lee, G., Olevsky, E. A., Maniere, C., Maximenko, A., Izhvanov, O., Back, C., McKittrick, J., "Effect of electric current on densification behavior of conductive ceramic powders consolidated by spark plasma sintering," *Acta Materialia*, 2017. doi: 10.1016/j.actamat.2017.11.010

17. Martirosyan, K. S and Luss, D., "Carbon Combustion Synthesis of Oxides Process Demonstration and Features," *AIChE*, Vol. J 51 10, 2005, pp. 2801−2810.

18. Markov, A. A., Hobossian, M. A., Martirosyan, K. S., "Investigation of the synthesis of ferrites behind the combustion wave using models of sliding and temperature jumps and concentrations of the components of the gas phase on the surface of the pores of the solid phase," *Physical-Chemical Kinetics in Gas Dynamics*, Vol. 16, No. 1, 2015. http://chemphys.edu.ru/issues/2015-16-1/articles/506/

19. Markov, A. A., Filimonov, I. A., and Martirosyan, K. S., "Synthesis simulation of submicron particles of complex oxides," *Theoretical Foundations of Chemical Engineering*, Vol. 1, 2017, pp. 1−12.

20. Markov, A. A., Filimonov, I. A., and Martirosyan, K. S., "Carbon Combustion Synthesis of Oxides: Effect of Mach, Peclet, and Reynolds Numbers on Gas Dynamics," *International Journal of Self Propagating High Temperature Synthesis*, Vol. 22, No. 1, 2013, pp. 11–17.

21. Markov, A. A., Filimonov, I. A., and Martirosyan, K. S., "Simulation of front motion in a reacting condensed two phase mixture," *J. Comput. Phys*., Vol. 231, No. 20, 2012, pp. 6714–6724.

22. Markov, A. A., "On Thermal and Mass Dispersion Effect on Barium Titanate Synthesis via CCSO," *Physical-Chemical Kinetics in Gas Dynamics*, Vol. 20, No. 4, 2019. http://chemphys.edu.ru/issues/2019-20-4/articles/870/

23. Markov, A. A., "On fine particles synthesis using three-zone reactor," August 2020. *J. of Physics: Conference Series*, 1611:012047, 2020. doi: 10.1088/1742-6596/1611/1/012047

24. Whitaker, S., "Transport equations for multi-phase systems," *Chemical Engineering Science*, Vol. 28, 1973, pp. 139−147.

25. Hsu, C. T., Cheng, P., "Thermal dispersion in a porous medium," *Int. J. Heat Mass Transf*., Vol. 33, 1990, pp. 1587–1597.

26. Fatehi, M., and Kaviany, M., "Role of gas-phase reaction and gas-solid thermal nonequilibrium in reverse combustion," *Int. Heat Mass Transfer*, Vol. 11, 1997, pp. 2607−20.

27. Oliveira, A. A. M., and Kaviany, M., "Nonequilibrium in the transport of heat and reactants in combustion in porous media," *Progress in Energy and Combustion Science*, Vol. 27, 2001, pp. 523−45.

28. Pereira, F. M., Oliveira, A. A. M., and Fachini, F. F., "Theoretical analysis of ultra-lean premixed flames in porous inert media," *J. Fluid Mech*., Vol. 657, 2010, pp. 285–307.

29. Fatehi, M., and Kaviany, M., "Role of gas-phase reaction and gas-solid thermal nonequilibrium in reverse combustion," *Int. Heat Mass Transfer*, Vol. 11, 1997, pp. 2607−2620.

30. Delgado, J. M. P. Q., "Longitudinal and transverse dispersion in porous media," *Chem. Eng. Res. Des., Elsevier*, Vol. 85, No. 9, 2007, pp. 1245–1252.

31. Sorokova, S. N., Knyazeva, A. G., "Associated model of sintering powders of the Ti-TiAI3 system," *Bulletin of the Tomsk Polytechnic University*. Vol. 314, No. 2, 2009, pp. 96−101.

32. Sorokova, S. N., Knyazeva, A. G., "Mathematical modeling of volumetric changes during sintering of powders of the Ti-Al system," *Physical mesomechanics*, Vol. 11, No. 6, 2008, pp. 95−101.

33. Markov, A., "Modeling the Synthesis of Barium Titanate Micron Particles in Axisymmetric Direct-Flow and Three-Zone Reactors," *J. Eng. Phys. Thermophy*, Vol. 94, 2021, pp. 1312–1325. https://doi.org/10.1007/s10891-021-02412-8

34. Markov, A. A., "Thermal and Concentration Expansion in the Synthesis of Barium Titanate in a Once-Through Reactor," *Theoretical Foundations of Chemical Engineering*, Vol. 55, No. 5, 2021, pp. 929–941.

35. Adachi, J., Kurosaki, K., Uno, M., and Yamanaka, S., "Thermal and electrical properties of zirconium nitride," *J. Alloys Compd.*, Vol. 399, No. 12, 2005, pp. 242–244.

36. Aigner, K., Lengauer, W., Rafaja, D., and Ettmayer, P., "Lattice parameters and thermal expansion of Ti(CxN^x), Zr(CxN^x), Hf(CxN1.x) and TiN^x from 298 to 1473 K as investigated by high-temperature X-ray diffraction," *J. Alloys Compd.,* Vol. 215, No. 1-2, 1994, pp. 121−126.

37. Markov, A. A., "Simulation of a two-stage reactor for the synthesis and sintering of ultrafine zirconium nitride," *Proceedings of the Twenty-second International Conference on Computational Mechanics and Modern Applied Software Systems (VMSPS'2021)*, Sept. 2021, Alushta, -. M. Publishing house MAI, pp. 411−413. ISBN 978-5-4316-0824-7 (in Russian).

38. Olevsky, E. A., "Theory of sintering: from discrete to continuum," *Mater. Sci. & Eng. R: Reports*, Vol. 23, No. 2, 1998, pp. 41−100.

39. Olevsky, E., Timmermans, G., Shtern, M., Froyen, L., and Delaey, L., "The permeable element method for modeling of deformation processes in porous and powder materials: Theoretical basis and checking by experiments," *Powd. Technol.*, Vol. 93, No. 2, 1997, pp. 123−141.

40. Anderson, K. R., Groza, J. R., Fendorf, M., Echer, C. J., "Surface oxide debonding in field assisted powder sintering," *Mat. Sci. Eng. A.*, Vol. 270, No. 2, 1999, pp. 278−282.

41. Markov, A. A., "Jump-Slip simulation technique for combustion in submicron tubes and submicron pores," *Computers and Fluids*, Vol. 99C, 2014, pp. 83−92.

42. Harrison, R., Rapaud, O., Pradeilles, N., Maitre, A., and Lee, W. E., "On the fabrication of ZrCxNy from ZrO2 via two-step carbothermic reduction-nitridation," *J. Eur. Ceram. Soc.*, Vol. 35, No. 5, 2015, pp. 1413−1421.

43. Xie, Z. Fu, Y. Wang, S., Lee, W., and Niihara, K., "Synthesis of nanosized zirconium carbide powders by a combinational method of sol-gel and pulse current heating," *J. Eur. Ceram. Soc.*, Vol. 34, No. 1, 2014, pp. 13e1−13e7.

44. Bardelle, Ph., and Warin, D., "Mechanism and kinetics of the uranium-plutonium mononitride synthesis," *J. Nucl. Mater.*, 1992, Vol. 188. doi: 10.1016/0022-3115(92)90451-p

45. Olevsky, E., Timmermans, G., Shtern, M., Froyen, L., and Delaey, L., "The permeable element method for modeling of deformation processes in porous and powder materials: Theoretical basis and checking by experiments," *Powd. Technol.*, Vol. 93, No. 2, 1997, pp. 123−141.

46. Ortega, A., Alcala, M. D., and Real, C., "Carbothermal synthesis of silicon nitride (Si3N4): kinetics and diffusion mechanism," *J. Mater. Process. Technol*., Vol. 195, No. 13, 2008, pp. 224−231.

47. Weimer, A. W., Eisman, G. A., Susnitzky, D. W., Beaman, D. R., and McCoy, J. W., "Mechanism and kinetics of the carbothermal nitridation synthesis of alpha-silicon nitride," *J. Am. Ceram. Soc.*, Vol. 80, No. 11, 1997, pp. 2853−2863.

48. Boley, Bruno A., Weiner, Jerome H., *Theory of Thermal Stresses*, Dover Civil and Mechanical Engineering Ser., Publisher: Dover Publications; Revised edition 2011, 608 p.

49. Conrad, H., "Electroplasticity in metals and ceramics," *Mat. Sci. Eng. A.*, Vol. 287, No. 2, 2000, pp. 276−287.

50. Olevsky, E., Tikare, V., and Garino, T., "Multi-scale modeling of sintering - A Review," *J. Amer. Ceram. Soc.,* Vol. 89, No. 6, 2006, pp. 1914−1922.

51. Frank-Kamenetskii, D.A., *Diffusion and Heat Transfer in Chemical Kinetics*, (Second Enlarged and Revised Edition), Translation Editor: J.P. Appleton, Plenum Press, 1969.

52. Markov, A. A. and Filimonov, I. A., "Model of thermal radiation using heat absorption by CO_2 in submicron pores with application to magnesium-zinc ferritefine disperse particles synthesis via combustion," *APhM 2017 IOP Publishing IOP Conf. Series: Journal of Physics: Conf. Series* 1009, 2018, 012040. doi :10.1088/1742-6596/1009/1/012040

List of principal notations

T_0	Referred temperature (K)
T'	Dimensional temperature
$T = \dfrac{T'}{T_0}$	Dimensionless temperature
$\tilde{T} = \dfrac{T-1}{\beta}$	Dimensionless normalized temperature
T_g, T_{jS}	Gas temperature and solid phase temperature
T_{init}	Temperature of combustion initiation
$T_{initial}$, $T_{initial} = -1/\gamma$	Initial temperature of the sample
c_{Pk}	Specific capacity at constant pressure $(\mathrm{J/kg/K})$
$\rho_{1g} = \rho_{N2}$, $\rho_{1s} = \rho_{Zr}$, $\rho_{2s} = \rho_{ZrN}$	Densities of gas and solid species $\left(\mathrm{kg\cdot m^{-3}}\right)$
$\rho_g = \rho_{1g} + \rho_{2g} + \rho_{3g}$	Density of gas mixture $\left(\mathrm{kg\cdot m^{-3}}\right)$
$v_{jS} = \dfrac{M_{jS}}{\rho_{jS}}$	Molar volume of solid component
$\omega = \displaystyle\sum_{k=1}^{3} \varepsilon_{kk}$	First invariant of deformation tensor (Pa)
σ_{ij}	Stress tensor for solid phase (Pa)
$\displaystyle\sum_k \sigma_{kk} = \left(2\mu_{S1} + 3\mu_{S2}\right)\sum_k \varepsilon_{kk} - 3K\omega$	Thermo-elasticity relation (Pa)
$\sigma_{ij} = 2\mu_{S1}\varepsilon_{ij} + \delta_{ij}\left(\mu_{S2}\displaystyle\sum_k \varepsilon_{kk} - K\omega\right)$	Duamel$-$Neuman formulas
$\omega = \omega_T + \omega_g + \omega_S$	Total expansion (dimensionless)
μ_{S1}, μ_{S2}	Lame coefficients (Pa)
ω_g, ω_S	Concentration expansions
ω_T	Thermal expansion (dimensionless)
E_1	Activation energy $\left(\mathrm{J\cdot mole^{-1}}\right)$

K	Volumetric expansion coefficient (Pa)
$\bar{\alpha}_{ig}$, $\bar{\alpha}_{iS}$	Species expansion coefficients (dimensionless)
$\beta_k = \dfrac{RT_0}{E_k}, k = 1,2$ $\gamma = \dfrac{c_P T_0 \beta_1}{Q_1}$	Dimensionless parameters
ε_{ij}	Tensor of deformations (dimensionless)
$\text{Pe}_l = \dfrac{u_0 l_0}{D_{l,0}}, l = 1,2$, $\text{Pe}_T = \dfrac{u_0 l_0}{\lambda_0}$	Peclet numbers (dimensionless)
$u_0 = \dfrac{l_0}{t_0}$	Referred velocity $\left(\text{m} \cdot \text{s}^{-1} \right)$
$\text{Re}_0 = \dfrac{u_0 l_0 \rho_0}{\mu_0}$	Reynolds number (dimensionless)
R_{Solid}	The Reynolds number analog for solid phase
χ	Porosity coefficient (dimensionless)
κ	Thermal transfer coefficient $\text{W} \cdot \text{K}^{-1} \cdot \text{m}^{-2}$
$P_0,$	Referred pressure (Pa)
μ_0	Referred gas viscosity $\left(\text{kg} \cdot \text{m}^{-1} \cdot \text{s}^{-1} \right)$
λ_0	Referred thermal conductivity $(\text{W} \cdot \text{m}^{-1} \cdot \text{K}^{-1})$
Ma_0	Mach number (dimensionless)
$M_{1g}, M_{2g}, M_{jS}, j = 1,2$	Molar masses $\left(\text{kg} \cdot \text{mole}^{-1} \right)$
Q_f	Thermal flux $(\text{W} \cdot \text{m}^{-2})$
$Q_r, k, \tilde{Q}_r = \dfrac{Q t_0 k}{\rho_0 C_{pg} T_0}, \tilde{k} = t_0 k$	Combustion heat and fate $(\text{W} \cdot \text{m}^{-2})$, (s^{-1})
Q_{Tg}, Q_{Ts}	Heat fluxes due to chemical reaction $(W \cdot m^{-2})$
Q	Creep activation energy in the power law $\left(\text{J} \cdot \text{mole}^{-1} \right)$

$\mathrm{Pe}_T = \dfrac{l_0^2 \rho_0 c_p}{t_0 \lambda_0}$	Peclet number for gas phase (dimensionless)
$\mathrm{Pe}_{Ts} = \dfrac{l_0^2 \rho_0 c_{ps}}{t_0 \lambda_s}$, $\mathrm{Pe}_{gr} = \dfrac{l_0^2 \rho_{gr} c_{p,gr}}{t_0 \lambda_{gr}}$	Peclet numbers for solid phases (dimensionless)
$\mathrm{Pe}_{el} = \dfrac{l_0^2 \rho_{el} c_{p,el}}{t_0 \lambda_{el}}$	Peclet number for wolfram tungsten (dimensionless)
Q_{Joul}	Joul's heat due to electric current in a tungsten channel $(\mathrm{W} \cdot \mathrm{m}^{-2})$
$\tilde{j} = \sigma_{el} E_{el,0}$	Electric current (A)
$j = \sigma E$, $\varphi_0 = l_0 E_{el,0}$	Electric current (A), electric potential (V)
$q_{g,rad}$	The thermal radiation / absorption heat flux $(\mathrm{W} \cdot \mathrm{m}^{-2})$
$A_W = \dfrac{2\chi l_0^2}{r_p} \dfrac{\sigma_B}{\lambda_0} T_0^3$, ε_Σ, $\dfrac{1}{\varepsilon_\Sigma} = \dfrac{1}{\varepsilon_g} + \dfrac{1}{\varepsilon_s}$	Boltzmann's constant, emissivity
D_T	Thermal diffusivity coefficient $(\mathrm{W} \cdot \mathrm{m}^{-1} \cdot \mathrm{K}^{-1})$
$R = 8.314$	Gas constant $(\mathrm{J} \cdot \mathrm{mole}^{-1} \cdot \mathrm{K}^{-1})$
t_{init}	Duration of thermal flux supply for combustion initiation
$q_f(t)$	External heat flux $(\mathrm{W} \cdot \mathrm{m}^{-2})$
N_{2f}	External nitrogen flux $(\mathrm{kg} \cdot \mathrm{m}^{-2} \cdot \mathrm{s}^{-1})$
$\dot{\gamma}$, $\dot{\gamma} = \dot{\gamma}_0 \exp\left(-\dfrac{Q}{RT}\right)$	Plastic deformation, densification rate
ΔG	Activation energy of plastic deformation, (kJ/mol)
$\varphi = (1-\chi)^2$	Normalized shear modulus (dimensionless)
$\psi = \dfrac{2}{3} \dfrac{(1-\chi)^3}{\chi}$	Normalized bulk modulus (dimensionless)

$\sigma(W)$	Equivalent stress for the power law, $\sigma(W) = A_m \cdot W^m$
$\sigma_{z,ole}$, $\dot{\chi}_{ole}$	Stress, densufucation rateusing model [41]
P_L	Effective stress of free sintering(dimensionless)
P_{ex}, P_g	External pressure, gas pressure at the pore boundary
$P_{tot} = P_{ex} - P_g$	Total pressure (Pa)
$\dot{\varepsilon}_{ij}$	Strain rate tensor(dimensionless)
A, A_0	Creep coefficients for the power law, $A_m = \dfrac{A_0 T}{r_p}\left(\dfrac{d}{b}\right)^p \exp\left(\dfrac{-Q}{RT}\right)$ (dimensionless)
$i_{elast}(t,x,r) = \begin{cases} 1, & \chi < \zeta\chi_0 \\ 0, & \chi \ge \zeta\chi \end{cases}$	Thermal elasticity/plasticity criteria (dimensionless)
$\zeta = \dfrac{\left(1-10^{-3}\right)G_1}{G_0}$	$G_1 = \dfrac{\rho_{2s}}{M_{2s}} - \dfrac{\rho_{1s}}{M_{1s}} - \dfrac{\rho_{1g}}{M_{1g}}$, $G_0 = \dfrac{\rho_{2s}^0}{M_{2s}} - \dfrac{\rho_{1s}^0}{M_{1s}} - \dfrac{\rho_{1g}^0}{M_{1g}}$
$\dfrac{r_P - r_P^0}{r_P^0} = 0.2\%$	Thermal elasticity/plasticity criteria for solid particle
$n_P = N_A \cdot V_P / V_0$	$n_P \left(\text{mol}^{-1}\right)$, $N_A = 6\times10^{23} \left(\text{mol}^{-1}\right)$
r_P, V_P	Radius, volume of solid particle, $r_P \approx 5\times10^{-7}\,(\text{m})$
Subscripts: g, s, zero	Gas, solid, initial value